AN ANALYTICAL METHOD FOR EVALUATING THE DEFLECTION AND LOAD-BEARING AND ENERGY ABSORPTION CAPACITY OF ROCKFALL RING NETS CONSIDERING MULTIFACTOR INFLUENCE

Li-Ping Guo [1, 2], Zhi-Xiang Yu [1, 2, 3, *], Yun-Tao Jin [1, 2], Lin-Xu Liao [1, 2] and Li-Ru Luo [1, 2]

[1] *School of Civil Engineering, Southwest Jiaotong University, Chengdu, China*

[2] *Research Centre for Protection Structures Against Natural Hazards, Southwest Jiaotong University, Chengdu, China*

[3] *Shock and Vibration of Engineering Material and Structure Key Laboratory of Sichuan Province, Mianyang, China*

* (Corresponding author: E-mail: yzxzrq@swjtu.edu.cn)

ABSTRACT

In this study, an analytical method for evaluating the structural performance, including maximum deflection, load-bearing, and energy absorption capacity of a steel wire-ring net, was proposed to effectively design the ring net of the flexible barrier systems. Puncture tests of the ring nets and two-point traction tests of the three-ring chains with various wire-ring specifications were conducted. Correlation analysis was used to test the results between ring nets and chains, revealing that three structural performance indicators of the test specimens were strongly related. The ring net's structural performance was affected specifically by ring chains on the shortest load transfer path. Accordingly, a three-ring chain with a flexible boundary corresponded to a fibre–spring element. A three-dimensional analytical model of the ring net was established. Explicit formulas for computing the three indicators of the ring net were derived. Comprehensive quasi-static and impact tests, using different shapes and sizes of punching devices, were conducted, providing valuable data to calibrate and validate this analytical method. The ability of the model in yielding consistent results when implemented at the structure scale was then assessed, based on the data of full-scale impact tests on a 1500kJ-energy rockfall barrier. Lastly, the effects of various factors, such as single ring geometry, the length–width ratio of the net, loading area size, boundary stiffness, and load rate, influencing the structural performance indicators of the ring net were investigated, respectively.

ARTICLE HISTORY

1.   Introduction

Flexible net barriers are protection structures used to mitigate geological hazards, such as rockfall [1,2], landslide [3], debris flow [4,5], and avalanche [6]. A typical flexible barrier mainly comprises the interception structure, support structure, connection components, and foundation. The flexible net panel is the key interception component of the protection system. When subjected to a falling rock impact, the out-of-plane puncture is a common failure mode of the net panel[7]. Once the net fails, the entire protective system may lose its protective function [8] (**Fig. 1**). Therefore, it is vital to study the puncture failure behaviour of the flexible net panel under the impact.

The maximum deflection [9], load-bearing capacity [10], and energy absorption capacity [11] are the three important indicators used to evaluate the flexible net panel's structural performance. Several experimental models have been developed over the past decades to investigate the structural performance of flexible net panels under out-of-plane loading. Quasi-static puncture tests were conducted on G.T.S mesh [12] and chain-link mesh [10]. The maximum deflection and the load-bearing capacity of the mesh are closely related to the loading area's size between the punch device and net panel. Further studies have shown that, with the same energy level, the smaller the loading area's size, the more prone to fail the mesh—the so-called "bullet effect" [13]. Rockfall impact tests conducted on ring nets with different boundary conditions have shown that boundary stiffness is also an important factor affecting its mechanical properties [14,15]. The more compliant the system, the larger the deformation ability and the higher impact resistance of the flexible barrier [16].

Various numerical approaches, using both FE [17] and DE [18] methods, for modelling rockfall protection systems with steel wire meshes have been proposed in the literature. A sophisticated numerical model [19,20] is well established for dynamic modelling of continuum problems with non-linear geometries, complex mechanical behaviour, and various contact conditions. However, such a process is time-consuming, especially if failure of the wire mesh and various load cases needs to be considered in practice.

A more efficient approach requiring fewer tests or lower computational costs is highly needed. Some researchers have also used theoretical methods to study the puncture resistance–mechanical properties of flexible nets [21,22]. A dimensionless model [23] and analytical model [24] for chain-link mesh laid the foundations to understand the bullet effect. Peila et al. [25] developed a macro-analytical model for designing wire ropes, steel posts, and anchor foundations in a rockfall protective barrier. However, the net is considered to act only as a structure distributing the force on the cables and the posts. Yu et al. [26,27] obtained an empirical expression for calculating the punching deformation of the

ring net. Guo et al. [28] established a simplified model for the deformation and load-bearing capacity of the ring net, but it is only applicable to the square mesh, and cannot consider the influence of the boundary stiffness.

(a) Perspective view
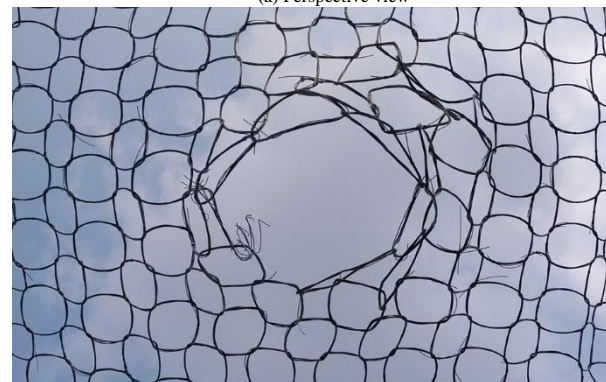
(b) Bottom view

Fig. 1 Failure of ring net

The above studies basically focus on a few factors on the energy absorption capacity of the net panel. The structural performance indicators of the actual steel-wire ring net are affected by multiple factors such as the strength of materials, the geometric parameters, the boundary stiffness, and the load rate.

However, comprehensive destructive tests and related analytical models of the steel-wire ring nets are rarely reported, which seriously affects the engineering design and application of flexible protection technology.

Aiming at effectively evaluating the maximum deflection, load-bearing, and energy absorption capacity of the steel wire ring net in the flexible barrier systems, out-of-plane puncture tests of the ring nets and 2-point traction tests of the three-ring chains with various wire-ring specifications were conducted. Correlation analysis was used to test results between ring nets and ring chains, revealing that three structural performance indicators of the test specimens were strongly related (**Section 2**). Multiple factors influencing the structural performance indicators of the ring net were summarized. The fundamental principles of mechanics were investigated in **Section 3**. The ring net's structural performance is especially affected by ring chains on the shortest load path of the ring net under out-of-plane load. Therefore, a three-ring chain with a flexible boundary on the load transfer path of the ring net was equivalented to a fibre–spring element. Then, a three-dimensional analytical model of the ring net was established (**Section 4**). Model parameters were calibrated by comparing analytical results to experimental tests performed at the wire-ring net scale

(**Section 5**). Additional quasi-static and impact tests, using different shapes and sizes of punching devices, were conducted, yielding valuable data to validate this analytical method. The ability of the model in yielding consistent results when implemented at the structure scale was then assessed, based on the data of full-scale impact tests on a 1500kJ-energy rockfall barrier. Lastly, the effects of multiple factors, such as single ring geometry, the length-width ratio of the net, loading area size, boundary stiffness, and load rate were studied (**Section 6**).

2. Model test

Different scales of single rings, ring chains, ring groups, and ring net panel specimens have been tested by [29–32], respectively. The above-mentioned studies could provide basic data for later research and reveal the mechanical behaviour of ring nets from different aspects. However, no studies are focusing on the relevance between test results of steel ring specimens with different scales, which would be insufficient to reveal the mechanical behaviour of the ring net in depth. Hence, this section focuses on investigating the relationships between ring nets and ring chains.
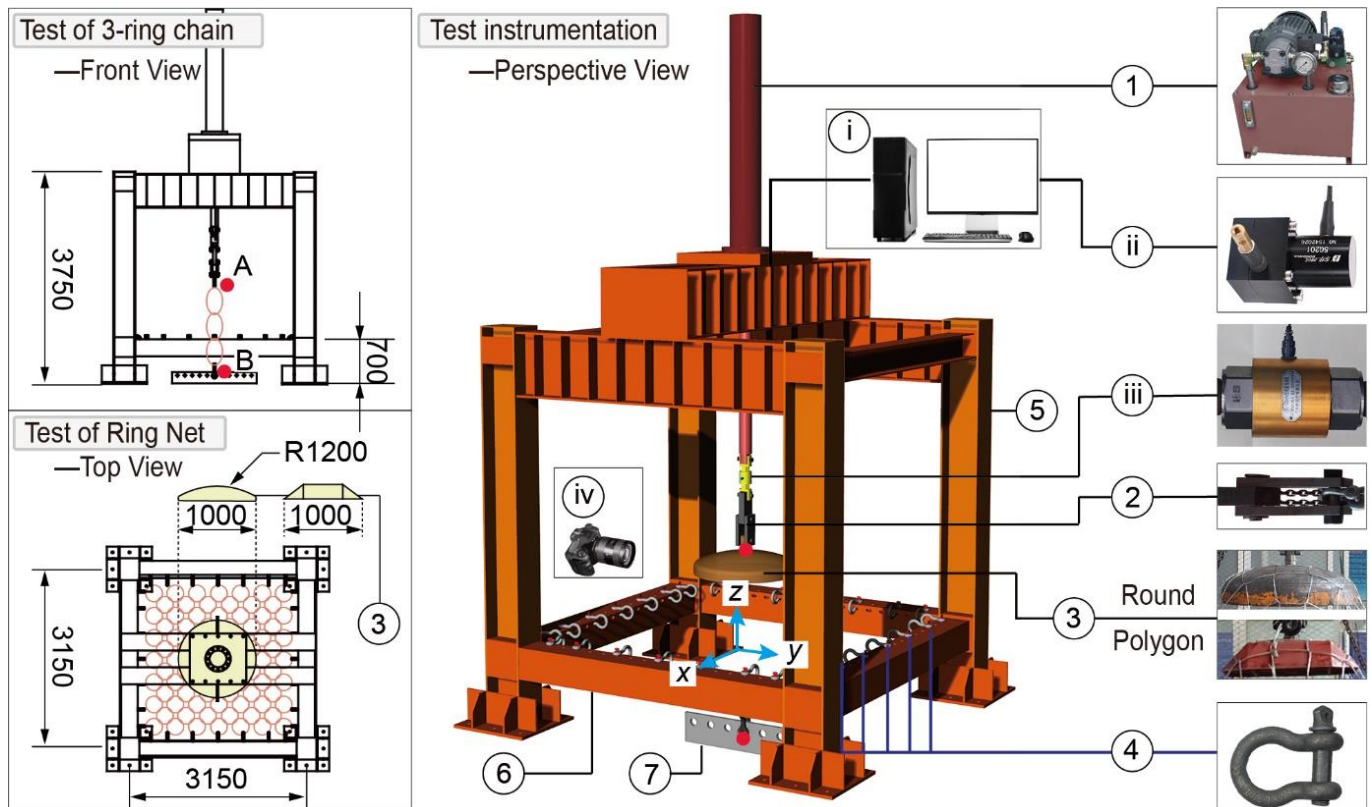

Fig. 2 Experimental setup and instrumentation

2.1. Experimental setup and instrumentation

The test site was located at the Rockfall Test Centre of Southwest Jiaotong University. The experiment setup was made of high-quality steel. The length and width of the steel frame were both 3.15 m, whereas the height was 3.75 m. The arrangement of the instrumentation is plotted in **Fig. 2**.

The test loading device included the following components and processes.

(1) A hydraulic loading system, comprising an electric motor and a hydraulic cylinder, is used to provide hydraulic power and pull the load device moving vertically with a speed of 7 ± 1mm/s.

(2) A connecting plate made of high-quality steel is used to connect the load sensor and the loading device.

(3) A polyhedral-shaped and hemispherical-shaped load sharing devices (press), respectively, correlate with the spherical block from the international standard [33] and the polyhedral block from [34] with different sizes of 600 mm and 1000 mm in diameter, are used to provide out-of-plane loading conditions to the ring net specimens.

(4) Shackles (8.5T~12.5T), symmetrically arranged along the lower beam, are used to anchor the net panel to the frame so that the boundary rings remained hinged.

(5) An I-shaped steel beam, with stiffener plates along the length direction, is used to transmit the load from the cylinder's hydraulic pressure to the ground.

(6) The lower beam, connected with shackles, is used to form the boundary conditions of the wire ring specimens. The horizontal plane of the ring net

boundary was used as the datum plane for measuring out-of-plane displacement.

(7) Hinged support, anchored at the centre of the steel frame bottom, is used to provide hinged constraints for the ring chains' specimens.

The instrumentation included the following.

(i) A data logger with the capability to sample 24 transducers at 1000Hz simultaneously is used to collect the transducer data.

(ii) A displacement sensor with 0.3%fs precision and a 1500mm measuring range are used to measure and record the out-of-plane displacement data.

(iii) A force sensor system with 0.3%fs precision and two types of measuring ranges (500kN and 1500kN) is connected in series with the punching device to measure the real-time tension force directly.

(iv) A video camera, with a resolution of 5184 × 3456 pixels and a frame rate of 30 frames per second is utilised to monitor the motion of the punch device and the deflection of the flexible barrier ring net during the out-of-plane loading.

2.2. Puncture test of the ring net

Firstly, out-of-plane puncture tests of the ring nets were conducted. To ensure the test's repeatability and the results' reliability, three identical ring nets are repeatedly tested for each specification. **Fig. 3** shows the ring net (RN) specification of RN07/3.0/300, which means the number of windings is $n_w = 7$, the diameter of the high-strength steel wire is $d = 3$ mm, and the average diameter of the single ring is $D = 300$ mm. Each ring net comprised 85 single rings, and the length and width of the net were 3m. **Table 1** shows all test

specimens of the ring nets. The net with the number of windings $n_w = 3$ and $n_w = 4$ is made of a high-strength steel wire with a diameter of $d = 2.2$ mm, while the net with $n_w \geq 5$ is made of a steel wire with diameter $d = 3.0$ mm.
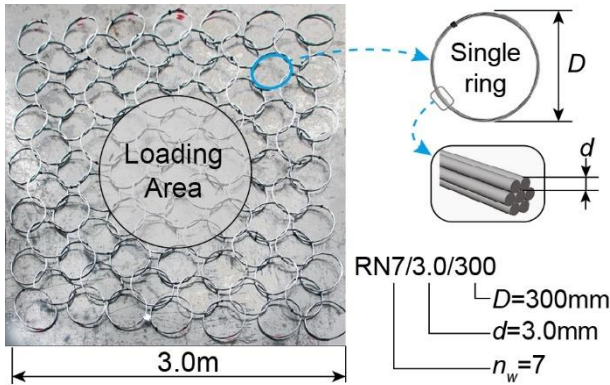

Fig. 3 Ring net specimen

Table 1
Specimens of steel wire-ring net panel

Test 1	Specification	Each ring in specimens		
		n_w	d	D
	RN03/2.2/300	3	2.2	300
	RN04/2.2/300	4	2.2	300
	RN05/3.0/300	5	3	300
Punching test	RN07/3.0/300	7	3	300
	RN09/3.0/300	9	3	300
	RN12/3.0/300	12	3	300
	RN16/3.0/300	16	3	300
	RN19/3.0/300	19	3	300

The out-of-plane puncturing tests on the net panels were conducted following the procedure suggested in the international standard [33]. The test comprised loading a net panel perpendicularly to its plane using the hemispherical-shaped loading device with a speed of 7 ± 1 mm/s and which was located centrally. Wire-ring net specimens were punctured upwards until failure. The force–displacement curve of the central point of the panel was then obtained. **Fig. 4** presents three typical deflection states at the representative time recorded by the side-view camera combined with the signal from load and displacement sensors.

From this figure, two occurring stages are obvious: When $t = t_0$, the initial moment, each ring in the net panel is kept in a round, which can be considered as being in a zero-stress state. At this moment, the bottom plane of the loading device is flush with the boundary plane of the ring net, and the out-of-plane displacement is recorded as $z = h_0$. At $t = t_1$, the wire rings have undergone a bending process, deforming to a rounded triangle and quadrilateral. The out-of-plane displacement is recorded as $z = h_1$. At $t = t_2$, the bending deformation of the ring has been fully developed. Steel wires are straightened and broken. The ring net panel is no longer able to support any increase to the applied force. At this moment, the out-of-plane deformation reaches the maximum $z = h_2$.
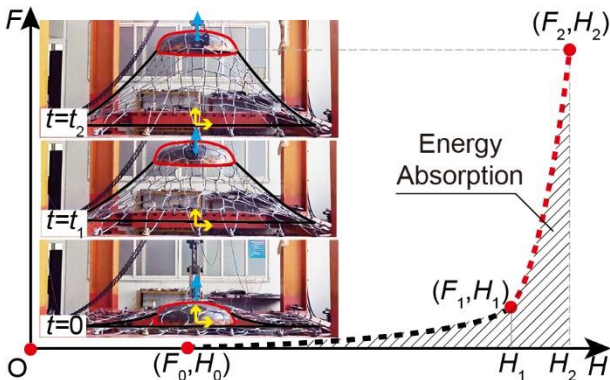
Corresponding to the pictures of the puncturing test, the traction force time-history curve shows obvious two-stage characteristics: In the first stage ($t_0 \sim t_1$), the out-of-plane displacement increases obviously (accounting for 85 % of the maximum defection), whereas the force increases slowly (accounting for 15 % of the puncture resistance). The traction force and displacement were recorded as F_1 and l_1, respectively, at t_1. In the second stage ($t_1 \sim t_2$), the displacement increases slowly (accounting for 15 % of the maximum deflection), whereas the force increases obviously (accounting for 85 % of the puncture resistance). The traction force and displacement were recorded as F_2 and l_2 respectively at t_2. The ring net failed at t_2, the out-of-plane deflection reached the maximum to $z = h_2$; and the tensile force reached the peak value of F_2.

The out-of-plane force and displacement signals were recorded in real-time by the load cell and the displacement sensor, respectively. The tension force doing work along the displacement direction was converted into internal energy and dissipated through the ring net.

2.3. Two-point traction test of the 3-ring chain

On the load transfer path of the ring net under out-of-plane load, steel rings are connected with each other, and typical test specimens with different scales, including single ring, ring chain, and ring group, appear concurrently. Among them, the ring chain is not only relatively simple but can also reflect the contact relationship between the steel rings and can represent the mechanical behaviour of other scale specimens.

To quantitatively describe the initial conditions, stiffness changes, and failure criterion of the steel rings in the net panel, 2-point traction tests on the 3-ring chains with the same number and specifications of ring net pieces were conducted. Also, the ultimate bearing capacity, maximum deflection, and energy absorption capacity of the three-ring chains were analysed respectively. **Table 2** shows all the 3-ring chain specimens. The 3-ring chain (RC) specification of RC07/3.0/300 means the number of windings is $n_w = 7$, the diameter of the high-strength steel wire is $d = 3.0$ mm, and the average diameter value of the single ring is $D = 300$ mm.

Table 2
Specimens of three-ring chain

Test 2	Specimens of ring chains	Each ring in specimens		
		n_w	d(mm)	D(mm)
	RC03/3.0/300	3	2.2	300
	RC04/3.0/300	4	2.2	300
	RC05/3.0/300	5	3	300
Two-point traction test	RC07/3.0/300	7	3	300
	RC09/3.0/300	9	3	300
	RC12/3.0/300	12	3	300
	RC16/3.0/300	16	3	300
	RC19/3.0/300	19	3	300

The 2-point traction test of the 3-ring chain was conducted following the procedure suggested in the international standard [33]. Before the test, a slight tension is given to stabilise the system; then, the force is reduced again to zero and the rings are kept round before the test started. The 3-ring chain was tensioned by the hydraulic loading rig with a displacement speed of 7 ± 1 mm/s, until breaking.
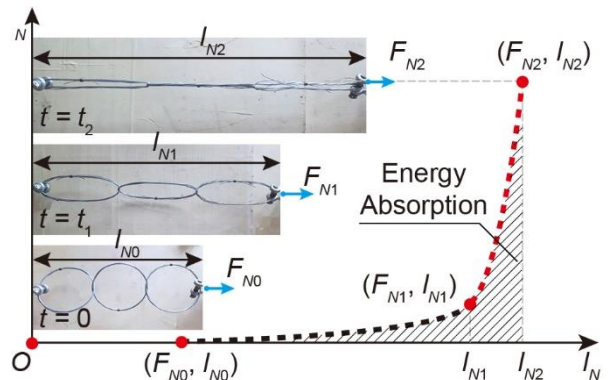

Fig. 4 Punching tests of the ring nets

Fig. 5 Two-point traction tests of the 3-ring chains

Fig. 5 shows three typical photos recorded by the camera combined with the load–displacement curve. At the initial moment($t = 0$), each ring in the three-ring chain is kept round, and the length of the ring chain is $l = l_0$. At $t = t_1$, the bending deformation of the net ring is fully developed and depicts an oval shape, with the chain length being $l = l_1$. At $t = t_2$, the ring chain is straightened, part of the steel wires of the ring at the contact position is broken, and the chain can no longer support any increase in the applied force. At this moment, the length of the ring chain reaches the maximum $l = l_2$.

Corresponding to the pictures of the 3-ring chain test, the traction force–displacement curve shows obvious two-stage characteristics. In the first phase ($0 \sim t_1$), the axial tension F_N slowly increases from 0 to F_{N1} (approximately 15% of the breaking load), and the length of the ring chain l_N increases significantly from l_{N0} to l_{N1} (approximately 85% of maximum deflection). In the second phase ($t_1 \sim t_2$), the axial tension force F_N of the net ring increases sharply from F_{N1} to F_{N2} (roughly 85% of breaking load), and the length of the ring chain l_N increases from l_{N1} to l_{N2} (nearly 15% of maximum deflection).

The traction force and displacement signals were recorded in real-time by the load cell and the displacement sensor, respectively. The tension force doing work in the displacement direction was converted into internal energy and dissipated through the 3-ring chain.
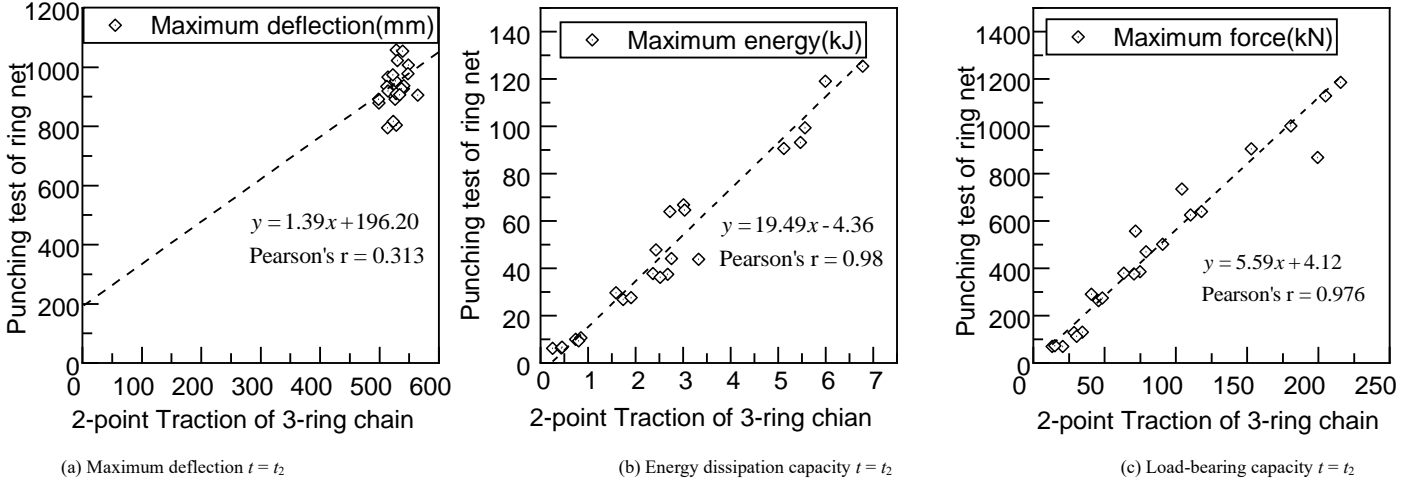

(a) Maximum deflection $t = t_2$

(b) Energy dissipation capacity $t = t_2$

(c) Load-bearing capacity $t = t_2$

Fig. 6 Correlation between test results of 3-ring chain and ring net

2.4. Correlation analysis

The same displacement-controlled loading condition, with a displacement speed of $7\text{mm} \pm 1\text{mm}$, was used for both the 2-point traction test of the 3-ring chain and the puncturing test of the ring net. Similar two-stage characteristics occurred on the force-displacement curves in both destructive tests of the ring nets and the 3-ring chains. The steel-wire rings were both deformed from a circular shape in the initial state to a straightened shape in the ultimate limit state. Furthermore, all the specimens eventually broke first at the point of contact where the rings underwent severe bending. To quantitatively study the correlation between the 3-ring chain and the ring net test results, the maximum deflection, load-bearing, and energy absorption capacity, Pearson's correlation coefficient was used to study the correlation relationship between the two tests, as Eq. (1) describes,

$$ r_{XY} = \frac{\sum_{i=1}^{n}\left(X_i - \bar{X}\right)\left(Y_i - \bar{Y}\right)}{\sqrt{\sum_{i=1}^{n}\left(X_i - \bar{X}\right)^2}\sqrt{\sum_{i=1}^{n}\left(Y_i - \bar{Y}\right)^2}} \tag{1} $$

where n is the sample size, X_i , Y_i are the values for each set of samples, $\bar{X}$ is the average value of X_i , and $\bar{Y}$ is the average value of Y_i .

Fig. 6 shows the correlation distribution between the 2-point traction test and the punching test results. Observably, there is no obvious correlation between the maximum deflection results, with a Pearson correlation coefficient of $r = 0.313$. However, the scattered plots are distributed in a small area, indicating that the breaking displacements are almost constant for all specimens of the 3-ring chain and ring net with different numbers of windings. The breaking force results of both tests showed a strong correlation, with the Pearson correlation coefficient of $r = 0.976$. The energy absorption results of the 3-ring chain and the ring net puncturing tests also show a strong correlation with the Pearson correlation coefficient of $r = 0.980$.

3. Fundamental concepts and principles of mechanics

3.1. Tension-bending coupling effects on the steel ring

Before breaking the steel wire rings in contact with each other, the wires underwent evident bending deformation in both puncturing and 2-point traction tests. Tension-bending coupling effects exist on the steel ring segment of the net. (**Fig. 7**). The dimensionless relationship form of the axial force-bending moment combined tension and bending of a circular member [35][24] is shown in Eq. (2),

$$ \frac{F_N}{F_y} = \frac{2}{\pi}\left\{\left(\frac{M}{M_y}\right)^{\frac{1}{3}}\sqrt{1-\left(\frac{M}{M_y}\right)^{\frac{2}{3}}} + \cos^{-1}\left[\left(\frac{M}{M_y}\right)^{\frac{1}{3}}\right]\right\} \tag{2} $$
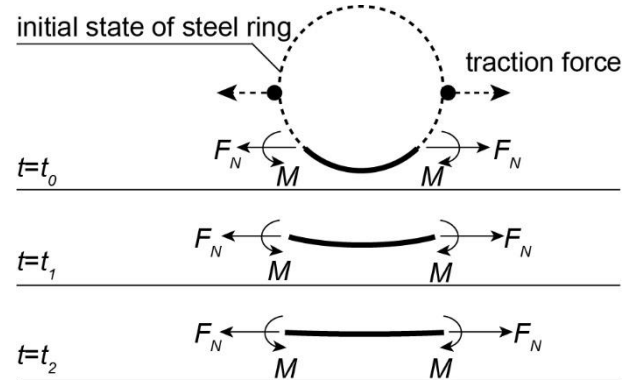

**Fig. 7** Deformation process of a steel ring segment

where M is the applied moment, and $M_y = \sigma_y d^3/6$ is the moment capacity of the wire in pure bending (zero tension). F_N is the applied axial force and $F_y = \sigma_y \pi d^2/4$ is the tensile bearing capacity of the wire in pure tensioning (zero bending). Eq. (2) demonstrates that bending deformation causes a potentially substantial reduction of the maximum axial force that the wire can sustain. On the left side of the equation, the normalised axial force F_N/F_y represents the degree of the axial force of the steel wire, which is simpler than the expression related to the bending moment on the right side. The development degrees of the axial force and bending moment of the ring section show an opposite tendency. When the degree of axial force development reaches the maximum, the axial force of the steel rings reaches the maximum. More generally, the dimensionless parameter γ_N could be defined below to express the development degree of the axial stress in the steel wire ring section (Eq. (3)).

$$ \gamma_N = F_N / F_y = \sigma_N / \sigma_y \tag{3} $$

Once the normalised axial stress ratio reaches the maximum that the contacted rings could sustain, the damage will occur on steel rings in the net.
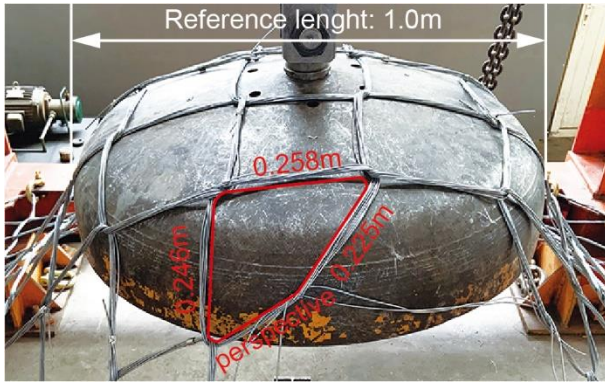
(a) Deformation pattern in loaded area
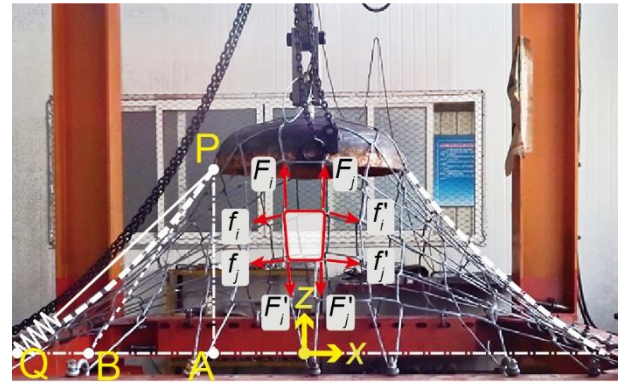
(b) Orthogonal internal force in load path

Fig. 8 Deformed steel rings at ultimate limit state

3.2. Load path of the ring net under out-of-plane load

Under out-of-plane loading, slippage occurred between the steel rings on the load path of the ring net. Each ring deformed due to the tension and bending force (**Fig. 8**). As the load increased, the deformation tended to stabilise, which limits the further development of sliding. Once the internal force of the ring section was along its axis, an obvious square-shaped pattern appears from the deformed rings in the loaded area between the net panel and load device. The dimension of the deformed rings on the loaded area was measured after out-of-plane loading. Although the bending of the rings was significant, there was a tiny difference in circumference before (942 mm) and after (959 mm) deformation, indicating that the tensile deformation of the rings was almost negligible.

An approximately orthogonal internal force distribution pattern of the deformed rings is formed on the load transfer path of the ring net. F_i and F_j are the internal force vectors of the steel rings stretched in the radial direction, while f_i and f_j are the internal force vectors of the rings stretched along the circumferential direction of the load device. Observably, the horizontal component of the internal force in the steel rings along the circumferential direction can be self-balanced, and that the vertical component is almost zero. The horizontal component of the internal force of the rings in the radial direction is self-balanced, and the vertical component is balanced with the out-of-plane load. Therefore, it is the radial internal forces in the ring chains around the punching device that form the main part of the bearing capacity of the steel wire-ring net panel.

The circumferential ring chains could influence those structural performances by creating a small off-angle of the load path (**Fig. 8 (b)**). Constrained by the circumferential ring chains, a curved load path is observed on the ring net (Arc PQ), and the tangent at the end of the curve should be the actual direction of the force vector in the fibre–spring element (Line PB). There is an off-angle ($\angle$ BPQ) of the force vectors between the analytical model and the experimental deformed ring net. These phenomena can be described using a correction coefficient:

$$\lambda_\theta = \angle APB / \angle APQ \tag{4}$$

3.3. Equilibrium of force system

At ultimate limit states, the steel rings on the load path of the net panel are fully stretched, and the internal axial force vectors of the radial ring chains were balanced with the out-of-plane loading (**Fig. 9**). The effect of the circumferential ring chains can be considered a correction coefficient to the direction of axial force in straightened rings (λ_θ). Further to the above analysis, considering the load-sharing device as a rigid block in 1D motion, the accelerating block can be transformed into an equivalent static system by adding the so-called d'Alembert inertia "force" ($\mathbf{I} = -m_{block}\mathbf{a}$). Thus, the space balance force system is formed between the out-of-plane load ($\mathbf{F}_{load}$), all internal axial force vectors of the rings, the block gravity, and the inertia force. As Eq. (5) describes,

$$\mathbf{F}_{load} + \mathbf{I} + m_{block}\mathbf{g} = -\sum \mathbf{F[i]} \cdot \mathbf{z} \tag{5}$$

where m_{block} is the mass of the block, $\mathbf{g} = 9.81 \text{m/s}^2$ is the gravitational acceleration, and $\mathbf{z}$ is the out-of-plane load direction of the rigid block. Keeping the same magnitude and direction of the force vector in the straightened rings, the complex force transfer path of the ring net can be replaced by tension-only fibres.
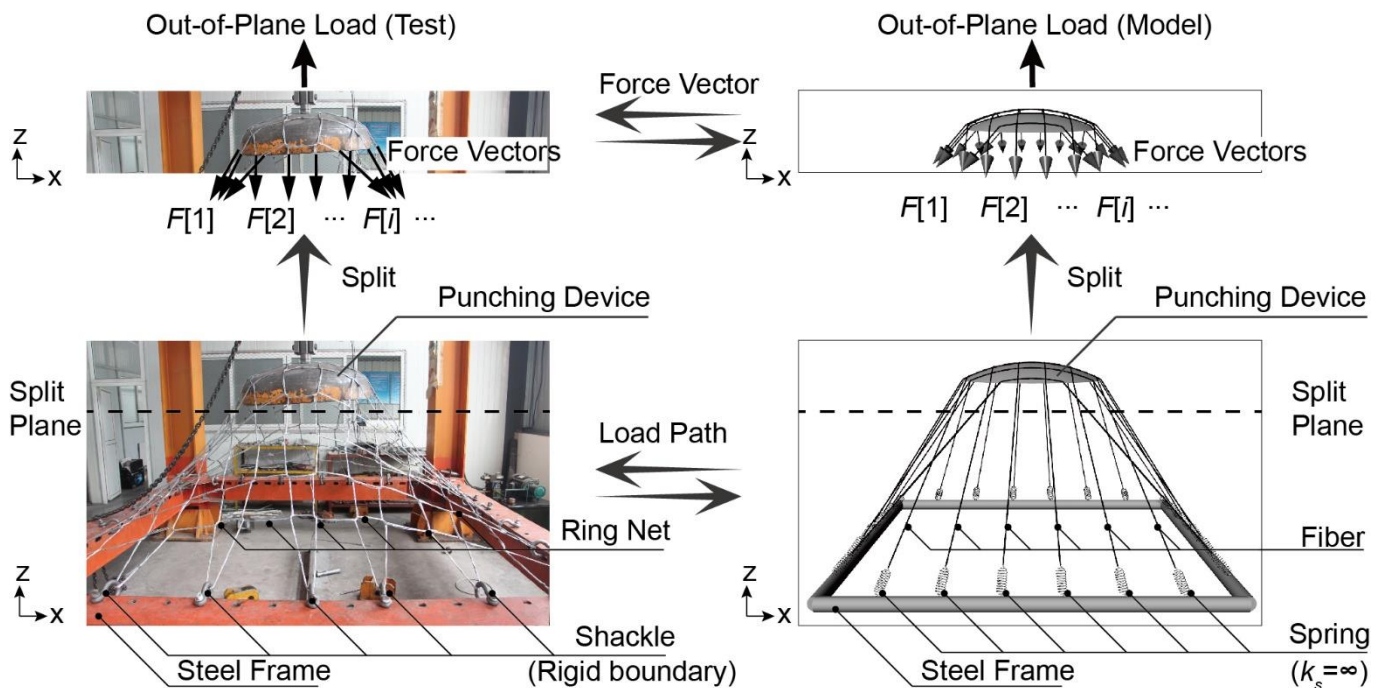

Fig. 9 Equivalent principle between the analytical model and the ring net under out-of-plane load

Once the axial stress factor γ_N of an equivalent fibre reaches its maximum value $\gamma_{N\max}$, the fibre is considered to have failed:

$$\gamma_N = \gamma_{N\max} \tag{6}$$

Rather than model the cables, posts, and foundations explicitly, the flexible boundary of the ring net can be represented by springs of some effective stiffness, as suggested by Spadari et al [36].

4. Analytical method

4.1. Key effects affecting structural behaviours

The influence of multiple factors is comprehensively reflected when the ring net in the flexible barrier system is impacted by a falling block. The main factors are summarized as follows:

(1) Material characteristics: The primary material of the ring net is a high-strength steel wire. The yield stress σ_y and diameter d of the steel wire are the main material parameters affecting the performance of the ring net.

(2) Steel ring specifications: The ring net panel is made of steel wire rings. The number of windings n_w and ring diameter D are the main parameters affecting the performance of the ring net.

(3) Loaded area (block): According to the "bullet effect"[13], the load-bearing capacity and maximum deflection of the ring net are directly related to the block size R_p and the diameter of the single ring D, which affects the number of tensioned rings at the edge of the loaded area. Also, the shape and position of the block are essential factors affecting net panel performance (**Fig. 10 a**).

(4) Geometry of the net panel: Rectangular ring net panel with different length–width ratios κ ($\kappa \geq 1$) could be used in actual engineering (**Fig. 10 b**). The ring net size should be determined by following the protective structure form and the spacing of the support structures. Once the width of the net is determined as w, the length would be κw. More steel wire rings may participate in the deformation and stress process with an increase in the ring net size, thereby affecting the performance of the whole ring net.

(5) Boundary stiffness: Generally, the ring net is supported with a steel column by wire ropes, which makes the boundary of the ring net flexible. The deformation of the wire ropes can affect the overall out-of-plane stiffness of the ring net. A boundary stiffness factor (k_s) can be used to evaluate the flexibility of the boundary and help calculate the deflection of the flexible ring net panel (**Fig. 10 c**).

(6) Load rate: The load rate of a flexible barrier in static and dynamic conditions differs. The variation in material strength with applied load rate should be considered in designing flexible barriers subjected to suddenly applied loads.

4.2. Fibre–spring element

From a structural engineering perspective, the energy absorption capacity of the ring chains under external loads is the area beneath the load-displacement curve under the assumption of reaching the failure load. The total energy absorbed by the steel rings is composed of elastic and plastic energy.

The axial mechanical behaviour of equivalent fibres should reflect the macro force–displacement relation of the ring segment under traction and ensure that the failure criterion, including the maximum length, breaking load, and energy absorption, is consistent with the segment in the ring chain test. Therefore, the two-stage force-displacement curve (**Fig. 5**) of the 3-ring chain is converted into the axial force–displacement curve of the equivalent fibres (**Fig. 11**).

The 3-ring chains bear traction force F_N, and the length of the 3-ring chain is l_N with an initial length of l_{N0}. The equivalent fibres bear axial force F_f, and the length is l_f with an initial length of l_{f0}. For a steel ring with n_w windings, the sectional area of both the ring chain and the equivalent fibres is A, it can be calculated as follows:

$$A = \frac{n_w \pi d^2}{4}, \quad l_{N0} = 3D \tag{7}$$

The fibre force–displacement curve can be divided into two stages: In the first stage, the axial force of the equivalent fibre (F_f) increases from 0 to $\gamma_{N1}\sigma_y A$, and the length of the equivalent fibre (l_f) increases from l_{f0} to l_{f1}, and the equivalent stiffness of the fibre is k_{f1}. In the second stage, the axial force F_f increases from $\gamma_{N1}\sigma_y A$ to $\gamma_{N2}\sigma_y A$, and the fibre length (l_f) increases from l_{f1} to l_{f2}. Also, the equivalent stiffness of the fibre is k_{f2}. The axial stress factor of the equivalent fibre γ_{N1} and γ_{N2} can be obtained from Eq. (8):

(a) loaded area

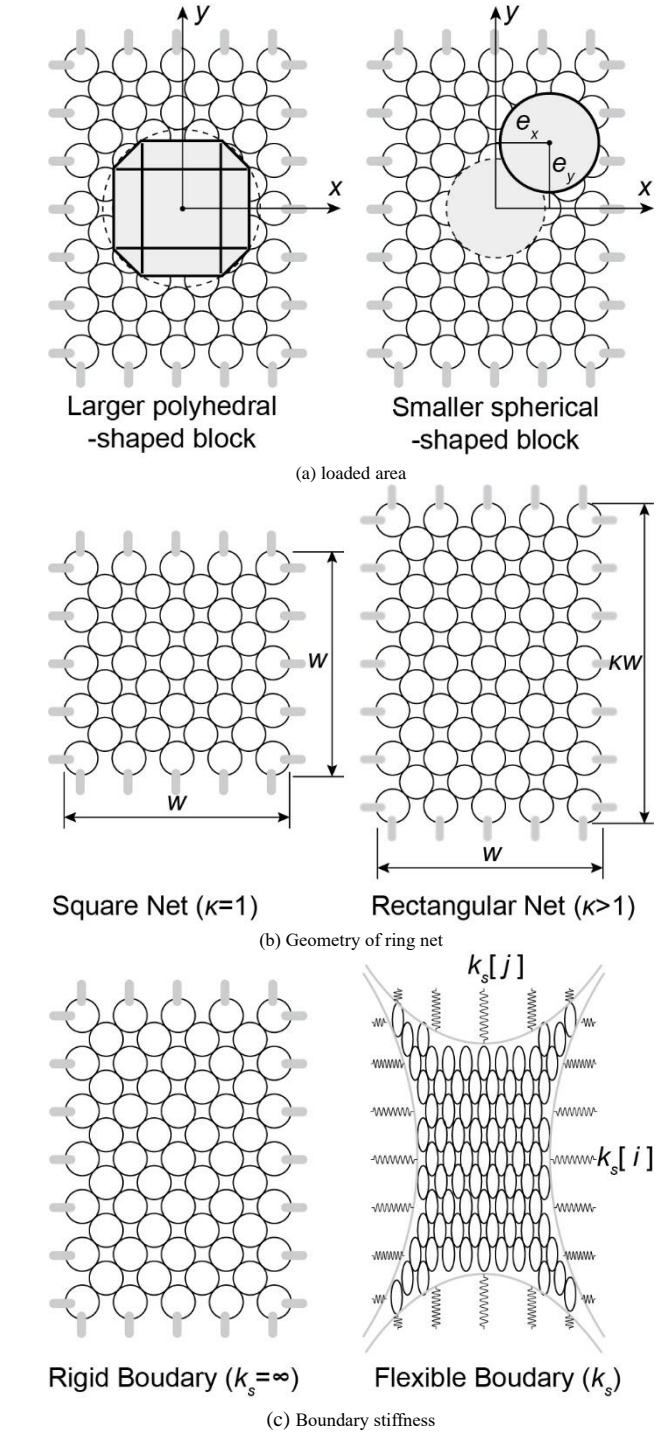
(b) Geometry of ring net

(c) Boundary stiffness

Fig. 10 Multiple-factor influence on ring net performance

$$\gamma_{N1} = \frac{F_{N1}}{2\sigma_y A}, \quad \gamma_{N2} = \frac{F_{N2}}{2\sigma_y A} \tag{8}$$

The equivalent stiffness and k_{f2} of the fibres can be calculated by Eq. (9).

$$k_{f1} = \frac{F_{N1} L_{N0}}{2(L_{N1} - L_{N0})l_{f0}}, k_{f2} = \frac{(F_{N2} - F_{N1})L_{N0}}{2(L_{N2} - L_{N1})l_{f0}} \tag{9}$$

Here, the differential force–displacement relationship of the equivalent fibre is defined by Eq. (10):

$$\frac{dF_f}{dl_f} = \begin{cases} k_{f1} & , 0 < \gamma_N \leq \gamma_{N1} \\ k_{f2} & , \gamma_{N1} < \gamma_N \leq \gamma_{N2} \end{cases} \tag{10}$$

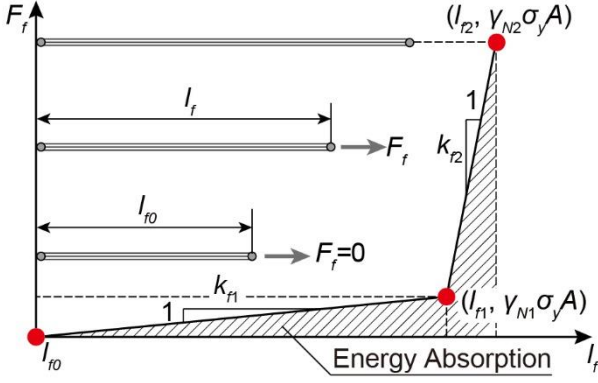with an initial condition of $F_f = 0$, $l_f = l_{f0}$.

Fig. 11 Equivalent force-displacement curve of the fibre

The equivalent springs bear axial force F_s, and the length is l_s. Then, the differential force-displacement relationship of equivalent spring with a constant stiffness k_s is defined by Eq. (11):

$$\frac{dF_s}{dl_s} = k_s \tag{11}$$

with an initial condition of $F_s = 0$, $l_s = l_{s0}$.

Since the fibre–spring element comprises equivalent fibre and spring in series, the axial force F of the element is equal to the equivalent fibre force F_f and the equivalent spring force F_s. The current length of the element L is the sum of the fibre length l_f and the spring length l_s, as Eq. (12) describes.

$$\begin{cases} F = F_s = F_f \\ L = l_s + l_f \end{cases} \tag{12}$$

where $F_f = \gamma_N \sigma_y A$

Combining Eqs. (10), (11), and (12), the force–displacement relationship of the fibre–spring model can be written as follows:

$$\frac{dF}{dL} = \begin{cases} K_1 = 1/\left(1/k_{f1} + 1/k_s\right), & 0 < \gamma_N \le \gamma_{N1} \\ K_2 = 1/\left(1/k_{f2} + 1/k_s\right), & \gamma_{N1} < \gamma_N \le \gamma_{N2} \end{cases} \tag{13}$$

With an initial condition of $F = 0$, $L = L_0 = l_{s0} + l_{f0}$. The overall stiffness of the fibre–spring element also has two-stage characteristics. When the development degree of the axial stress ranges in $0 \le \gamma_N \le \gamma_{N1}$, the fibre–spring element stiffness is K_1, and the overall stiffness of the fibre–spring element of the fibre–spring element is K_2 when the development degree of axial stress ranges in $0 \le \gamma_{N1} \le \gamma_{N2}$.

With the elongation of the fibre–spring element under axial loading, the work is converted to energy in the fibre–spring element. The relationship between the increment of the work E done by external forces and the increment of the element length can be written as follows:

$$\frac{dE}{dL} = \begin{cases} K_1(L - L_0), & 0 < \gamma_N \le \gamma_{N1} \\ K_1(L_1 - L_0) + K_2(L - L_1), & \gamma_{N1} < \gamma_N \le \gamma_{N2} \end{cases} \tag{14}$$

With an initial condition of $E = 0$, $L = L_0 = l_{s0} + l_{f0}$. Where L_1 is the length of the fibre–spring element when $\gamma_N = \gamma_{N1}$, which can be calculated by Eq. (15)

$$L_1 = L_0 + \frac{\gamma_{N1} \sigma_y A}{K_1} \tag{15}$$

When the axial stress level γ_N reaches its maximum γ_{Nmax}, the fibre–spring element fails immediately.

4.3. Analytical model

An equivalent analytical model of the ring net can be established as shown in **Fig. 12**. The fibre–spring elements are distributed at the edge of the loaded area. Under out-of-plane loading, the equivalent fibre and spring undergo axial deformation concurrently, forming the out-of-plane deflection of the ring net. For the present, the analytical model shall be restricted to a three-dimensional Cartesian coordinate, pictured as a set of three orthogonal x, y, and z axes.

As mentioned in **Section 3.2**, the deformed rings in the loaded area of the net panel have a square-shaped pattern, and the difference in circumference before and after deformation was almost negligible. It is assumed that the steel rings distributed in the loaded area deform to a regular rectangle after bending and straight deformation, and the dimensions of the deformed rings are determined by the geometric boundary (the length κw and width w) of the net panel, that is

$$2(1 + \kappa)a = \pi D \tag{16}$$

In the analytical model, the two sets of endpoints of the fibre–spring elements are located at the edge of the loading area and the geometric boundary of the ring net. Considering hemispherical-shaped and polygonal-shaped blocks, the external contour lines of the blocks are divided by deformed rectangular rings, producing a series of intersection points along the upper edge of the loaded area. The number of all fibre–spring elements is determined by these points. For brevity and focus, greater emphasis was placed on modelling the ring net panel subjected to out-of-plane loading by a hemispherical-shaped block in this study.

Let m be the total number of all fibre–spring elements, m_1 be the number of elements along the positive x-axis, and m_2 be the number of elements along the positive y-axis, then

$$\begin{cases} m_1 = \text{Round}\left[R_p / a\right] \\ m_2 = \text{Round}\left[R_p / (\kappa a)\right] \end{cases} \tag{17}$$

where Round[·] is a rounding function. Considering the bi-axial symmetry of the analytical model, the total number of all fibre–spring elements m can be calculated by

$$m = 2(m_1 + m_2) \tag{18}$$

A set of endpoints P_1, P_2 … P_i … P_{m1}, connecting with equivalent fibres of the fibre–spring elements are distributed along the upper edge of the load device, and another set of endpoints, Q_1, Q_2 … Q_i … Q_{m1}, connecting with equivalent springs of the fibre–spring elements, are distributed along the lower boundary of the ring net. For a random position of the loaded area centre with different shifts (e_x, e_y) along the x-axis and y-axis of the net panel (**Fig. 10 a**), the coordinates of P_i can be expressed as

$$\begin{cases} x_P[i] = a(i - 1/2) + e_x \\ y_P[i] = \sqrt{R_p^2 - a^2(i - 1/2)^2} + e_y \\ z_P[i] = z \end{cases} \tag{19}$$

The coordinates of Q_i can be expressed as

$$\begin{cases} x_Q[i] = \kappa w(i - 1/2)/(2m_1 + 1) + e_x \\ y_Q[i] = w/2 + e_y \\ z_Q[i] = 0 \end{cases} \tag{20}$$

where $i = 1, 2, \ldots m_1$, and all of the coordinate value in Eqs. (19) and (20) should be positive, that is $x_P[i] \ge 0$, $y_P[i] \ge 0$, $z_P[i] \ge 0$, $x_Q[i] \ge 0$, $y_Q[i] \ge 0$ and $z_Q[i] \ge 0$.

Along the x-axis, Each direction vector of the internal force of the fibre–spring element can be expressed as

$$\mathbf{PQ} = \left(x_Q[i] - x_P[i], y_Q[i] - y_P[i], -z\right) \tag{21}$$

The length of each fibre–spring element is defined by:

$$L[i] = |\mathbf{PQ}| \tag{22}$$

and the initial length of ith fibre–spring element is defined by:
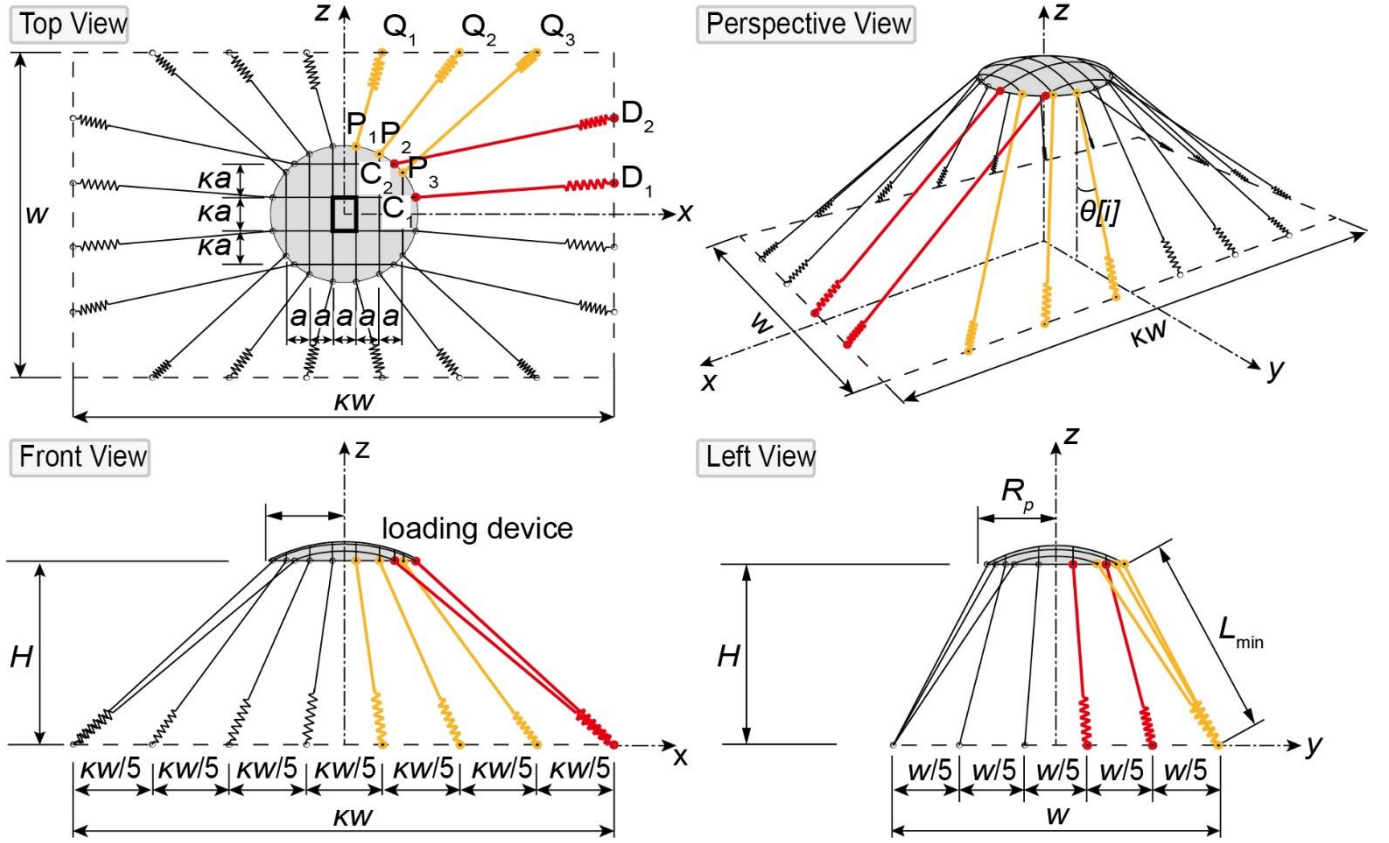
$$L_0[i] = |\mathbf{PQ}|\big|_{z=0} \tag{23}$$

Fig. 12 Geometric parameters of the analytical model

At any moment, the equivalent fibre length l_f and the spring length l_s in the fibre–spring element can be calculated by Eqs. (24) and (25), respectively.

When the axial stress level ranges in $0 < \gamma_N \leq \gamma_{N1}$,

$$\begin{cases} l_s[i] = \dfrac{k_{f1}[i]\big(L[i]-l_{f0}[i]\big)+k_s l_{s0}}{k_s+k_{f1}[i]} \\ l_f[i] = \dfrac{k_s\big(L[i]-l_{s0}\big)+k_{f1}[i]l_{f0}[i]}{k_s+k_{f1}[i]} \end{cases} \tag{24}$$

and when axial stress level ranges in $\gamma_{N1} < \gamma_N \leq \gamma_{N2}$

$$\begin{cases} l_s[i] = \dfrac{k_{f2}[i]\big(L[i]-l_{f1}[i]\big)+k_s l_{s1}[i]}{k_s+k_{f2}[i]} \\ l_f[i] = \dfrac{k_s\big(L[i]-l_{s1}[i]\big)+k_{f2}[i]l_{f1}[i]}{k_s+k_{f2}[i]} \end{cases} \tag{25}$$

where l_{f1} and l_{s1} are the length of the equivalent fibre and spring in the fibre–spring element when $\gamma = \gamma_{N1}$. The internal force of the ith fibre–spring element can be obtained by Eq. (26).

$$F[i] = \begin{cases} K_1[i]\big(L[i]-L_0[i]\big), 0 < \gamma_N \leq \gamma_{N1} \\ K_1[i]\big(L_1[i]-L_0[i]\big) \\ \quad +K_2[i]\big(L[i]-L_1[i]\big), \gamma_{N1} < \gamma_N \leq \gamma_{N2} \end{cases} \tag{26}$$

Integrating Eq. (14), the energy absorbed by the i-th fibre–spring element during the loading process can be obtained by:

$$E[i] = \begin{cases} K_1[i]\big(L[i]-L_0[i]\big)^2/2 & ,0 < \gamma_N \leq \gamma_{N1} \\ K_1 L_1[i]\big(L_1[i]-L_0[i]\big)+K_1\big(L_0^2[i]-L_1^2[i]\big)/2 & ,\gamma_{N1} < \gamma_N \leq \gamma_{N2} \\ \quad +K_2\big(L[i]-L_1[i]\big)^2/2 \end{cases} \tag{27}$$

As the symmetry of the model, the points, C_1, C_2 ... C_j ... C_{m2}, connecting with equivalent fibres of the fibre–spring elements in y-axis are distributed along the upper edge of the load device, and another set of endpoints, D_1, D_2 ... D_j ... D_{m2}, connecting with equivalent springs in the y-axis of

the fibre–spring elements, are distributed along the lower boundary of the ring net. Similarly, the coordinates of C_j can be expressed as:

$$\begin{cases} x_C[j] = \sqrt{R_p^2-(\kappa a)^2\big(j-1/2\big)^2}+e_x \\ y_C[j] = \kappa a\big(j-1/2\big)+e_y \\ z_C[j] = z \end{cases} \tag{28}$$

The coordinates of D_j can be expressed as:

$$\begin{cases} x_D[j] = \kappa w/2+e_x \\ y_D[j] = w\big(j-1/2\big)/\big(2m_2+1\big)+e_y \\ z_D[j] = 0 \end{cases} \tag{29}$$

where $j = 1, 2, ... m_2$, and all of the coordinate value in Eqs. (28) and (29) should be positive, viz. $x_C[j] \geq 0$, $y_C[j] \geq 0$, $z_C[j] \geq 0$, $x_D[j] \geq 0$, $y_D[j] \geq 0$ and $z_D[j] \geq 0$.

Along the y-axis, each direction vector of the internal force of the fibre–spring element can be obtained by

$$\mathbf{CD} = \big(x_D[j]-x_C[j], y_D[j]-y_C[j], -z_C\big) \tag{30}$$

The length of each fibre–spring element can be calculated by

$$L[j] = |\mathbf{CD}| \tag{31}$$

The initial length of each vector is defined by

$$L_0[j] = |\mathbf{CD}|\big|_{z=0} \tag{32}$$

The internal force value $F[j]$ and energy absorbed $E[j]$ of each element can be calculated by Eqs. (13) and (14), respectively. Once the axial force of any element in the analytical model develops to the maximum, the ring net panel is considered to fail.

$$\max\big\{|F[i]|, |F[j]|\big\} = \gamma_{N\max}\sigma_y A \tag{33}$$

When the load device moves to a certain height, it can be proved that the shorter the initial length $L_0[i]$ of the fibre–spring elements, the larger the axial

force $F[i]$ of the fibre–spring element. The proof process is as follows:

when $0 < \gamma_N \leq \gamma_{N1}$:

$$F = K_1(L - L_0) = k_s k_{f1} \frac{\sqrt{(l_{f0} + l_{s0})^2 + z^2} - (l_{f0} + l_{s0})}{k_{f1} + k_s}$$

where $L_0 = l_{f0} + l_{s0}$ and $l_{s0} = $const , then:

$$\frac{\partial F}{\partial L_0} = \frac{\partial F}{\partial l_{f0}} = -k_s k_{f1} \left(\sqrt{L_0^2 + z^2} - L_0 \right) \frac{k_{f1} + k_s + k_s \sqrt{L_0^2 + z^2} / l_{f0}}{(k_{f1} + k_s)^2 \sqrt{L_0^2 + z^2}} < 0$$

Similarly, it can be obtained that $\partial F / \partial L_0 < 0$ when $\gamma_{N1} < \gamma_N \leq \gamma_{N2}$.

This indicates that F is a decreasing function of L_0 . When the out-of-plane deflection reaches z , the smaller the initial length of the fibre–spring element, the larger the axial force $F[i]$. The maximum axial force $F[i=1]$ appears at the fibre–spring element $L_0[i]$ with a minimum initial length, and the failure occurs first on it, that is

$$L_0[i] < L_0[j] \Rightarrow F[i] < F[j] \tag{34}$$

The minimum initial length of the first failed element equals

$$L_0 \big|_{i=1} = \min \{ L_0[i], L_0[j] \} \tag{35}$$

For a ring net panel under out-of-plane loading, the maximum internal force of the shortest fibre–spring element ($i = 1$) fast develops and is the first to fail, which can be represented as follows:

$$F \big|_{i=1} = \gamma_{N2} \sigma_y A \tag{36}$$

Substituting Eq. (36) into Eq. (26), the maximum length of the shortest element that fails at first can be calculated by

$$L_{\max} \big|_{i=1} = L_0 \big|_{i=1} + \sigma_y A \left(\frac{\gamma_{N1}}{K_1 \big|_{i=1}} + \frac{\gamma_{N2} - \gamma_{N1}}{K_2 \big|_{i=1}} \right) \tag{37}$$

where L_0 is the fibre–spring element length at $z = 0$ and $L_{\max}$ at $z = H$, H_{net} represents the maximum out-of-plane deflection of the ring net. The three sides of H_{net} , $L_{\max}$, and L_0 forms a right triangle. According to the Pythagorean theorem, the maximum out-of-plane deflection H_{net} can be written as

$$H_{net} = z = \sqrt{L_{\max}^2 \big|_{i=1} - L_0^2 \big|_{i=1}} \tag{38}$$

Substituting Eq. (38) into Eq. (19), then the internal force vectors of $F[i]$ and $F[j]$ of each fibre–spring element, and the energy of $E[i]$, $E[j]$ absorbed can be calculated by Eqs. (26) and (27) respectively. Finally, the load-bearing capacity of the steel ring net F_{net} can be derived by projecting all force vectors in the z-axis:

$$F_{net} = 4 \left\{ \sum_{i=1}^{m_1} F[i] \cos(\lambda_\theta \theta[i]) + \sum_{j=1}^{m_2} F[j] \cos(\lambda_\theta \theta[j]) \right\} \tag{39}$$

where θ is the angle between the direction of the internal force vector of the fibre–spring element and the z-axis, and

$$\cos \theta[i] = \frac{H}{L[i]}, \cos \theta[j] = \frac{H}{L[j]} \tag{40}$$

Considering the influence of circumferential ring chains, the correction coefficient λ_θ has been calibrated through the test results (**Section 5.2**). Because of the scalar nature of energy, the energy absorption capacity of the ring net can be obtained by simply adding together values of energy dissipated by all fibre–spring elements, as Eq. (41) describes

$$E_{net} = 4 \left\{ \sum_{i=1}^{m_1} E[i] + \sum_{j=1}^{m_2} E[j] \right\} \tag{41}$$
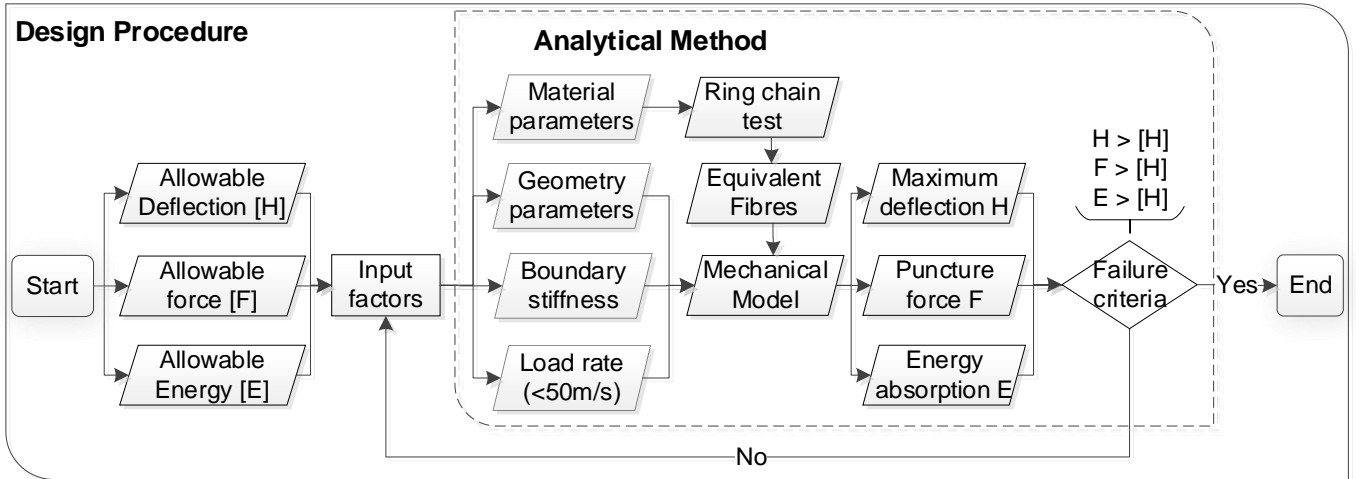

Fig. 13 Flowchart of the design procedure

4.4. Design procedure of the ring net

Through the analytical method, on the one hand, while it can be used to quantitatively analyse and evaluate the structural performance indicators of maximum out-of-plane deflection, load-bearing capacity, and energy absorption capacity of the ring net under multiple influence factors, it is convenient for designing the ring net in a specific engineering project.

The flowchart of the design procedure is depicted in **Fig. 13**. The design approach first entails an assessment of site conditions: characterization of the location, protective area, and allowable deflection of the flexible barrier and evaluation of the potential loads and gravitational energy that the ring net must withstand. Following this assessment, the geometry of the steel rings, loaded area, and the net panel are determined. The force-displacement relationship of the equivalent fibre is obtained through a three-ring chain test. The remaining parameters, such as the strength of the material, and boundary stiffness, are initially set as reference values. Then, a prototype of the ring net is developed. Using the analytical method, the maximum deflection, load-bearing, and energy

absorption capacity of the prototype are quantified to check whether its structural performance meets the protection requirements. If any of the calculated values is less than the allowable value, the influencing factors are adjusted, and the iteration process is activated until the correct design parameters are obtained.

5. Model parameters and calibration

In this section, the normalised axial stress ratio, the correction coefficient of the direction of force vectors, and stiffness of the equivalent springs for the analytical model are analysed and calibrated.

5.1. Normalised axial stress ratio

The experimental and literature results of the three-ring chain under quasi-static tension are used to calibrate the normalised axial stress ratio. Taking the specification of the ring chain as abscissa, the maximum axial stress ratio γ_{Nmax} as ordinate, and the scatter diagram is shown in **Fig. 14**. Observably, with an

increase in the number of windings of the ring net, both the experimental and literature results of the maximum axial stress ratio of the steel wire tend to increase. To quantify the relationship between the axial stress level of the steel wire and the number of windings of the ring, a linear fitting was performed on the scattered points, and a confidence band with a confidence level of 95% was drawn. Since n_w and γ_{Nmax} are dimensionless numbers, the relationship between the maximum axial stress levels γ_{Nmax} and n_w can be directly expressed by

$$\gamma_N = C_1 + C_2 n_w \tag{42}$$

Keeping γ_N in the confidence band, different C_1 and C_2 were tested until the strongest consistency between the experimental and calculated structural performance indicators of the ring net was achieved (**Fig. 17**), when $C_1 = 0.3$, $C_2 = 0.01$.
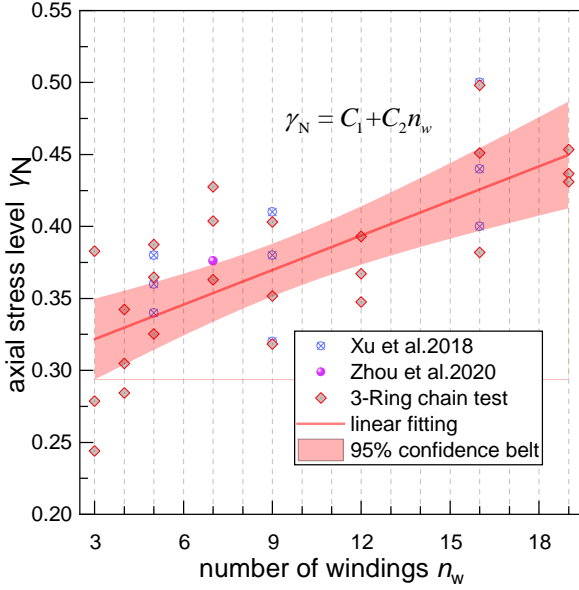

Fig. 14 Maximum normalized axial stress ratio in literature and ring chain tests **[30,32]**

5.2. Correction coefficient λ_θ

Puncture test results with rigid boundary and flexible boundary were conducted to calibrate the correction coefficient. The angles between the actual load path and the z-axis and between the fibre–spring element and the z-axis at the limit state were measured. **Table 3** shows the ranges of $\angle$ APB and $\angle$ APQ in the tests and the average correction coefficients.

Table 3
Statistical result of the off-angle in puncture tests

Puncture test	$\angle$APB	$\angle$APQ	Average $\lambda_\theta[i]$
Test2 (RN3-4)	27°~33°	43°~46°	0.73
Test2 (RN5-19)	29°~36°	44°~51°	0.71
Test-Po10R7	31°~33°	45°~48°	0.69
Test-Ro06R5	26°~31°	45°~48°	0.6
Test-Po06R7	22°~27°	44°~47°	0.58
Test-RN5Rope	21°~25°	36°~39°	0.61

Accordingly, correction coefficients between 0.5 and 0.75 were tested until $\lambda_\theta = 0.65$, where the calculated results properly agreed with the test results. Notably, assuming the angle $\angle$ APQ is 45 degrees, a correction coefficient λ_θ of 0.65 means that the force component along the z-axis would increase by 1.23 times that of the original fibre–spring element caused by the angle deviation ($\angle$ BPQ). A detailed description of the Test-Ro06R5, Test-Po06R7, Test-Po10R7, and Test-RN5Rope tests can be found in **Section 6**.

5.3. Boundary stiffness

In general, the boundary conditions of the ring net specimens in the quasi-static puncture tests differ in the actual rockfall barrier. In the puncture test, the ring net is connected with rigid shackles mounted to the steel frame so that the

boundary can be regarded as a "rigid boundary", i.e.

$$k_s = \infty \tag{43}$$

The ring net is usually connected to the support post by deformable wire ropes in the actual flexible barrier. According to the studies by [21], steel wire rope in a flexible barrier undergoes a nonlinear deflection process subjected to out-of-plane loads. If the drag force in steel rings is equivalent to the distributed load, the deformed wire rope geometry can be reduced to a parabola equation, which can explicitly be written as

$$y_r = \frac{4v_r}{l_{r0}^2}\left(l_{r0}x_r - x_r^2\right) \tag{44}$$

where l_{r0} and v_r are the lengths of the parabola along the x_r-axis and y_r-axis, respectively (**Fig. 15**). The maximum deflection v_r of the rope can be obtained by

$$v_r = \sqrt[3]{\frac{3q_e l_{r0}^4}{64 E_r A_r}} \tag{45}$$

where E_r is the elastic modulus, and A_r is the cross-sectional area of the rope. The flexible boundary (rope) is equivalent to several springs with a stiffness of k_s. Since the springs are connected in series with fibres to form the fibre–spring elements, the equivalent distributed load q_e along the wire rope depends on the number and magnitude of the internal force in the equivalent fibres. Let m_r be the number of fibre–spring elements, the maximum axial force in the fibres is $\gamma_{Nmax}\sigma_y A$. Then, q_e can be obtained by

$$q_e = \lambda_q \cdot \frac{m_r \gamma_{Nmax} \sigma_y A}{l_{r0}} \tag{46}$$

When failure occurs on the ring net panel, the axial stress ratio of the fibre–spring element on the shortest load path reaches its maximum γ_{Nmax}, but not all elements reach γ_{Nmax}, so a reduction coefficient λ_q is introduced in Eq. (46) to calculate the actual equivalent distributed load on the wire rope. Integrating Eq. (44), the arc length of the deformed rope can be obtained by

$$l_r = \sqrt{\frac{l_{r0}^2}{4} + 4v_r^2} + \frac{l_{r0}^2}{8v_r}\sinh^{-1}\left(\frac{4v_r}{l_{r0}}\right) \tag{47}$$

The internal force of the wire rope can be calculated by,

$$T_r = T_{r,x}\sqrt{1 + \left(\frac{q_e l_{r0}}{2T_{r,x}}\right)^2} \tag{48}$$

where $T_{r,x}$ is the horizontal component of T_r,

$$T_{r,x} = \frac{E_r A_r}{l_{r0}}\left(l_r - l_{r0}\right) \tag{49}$$
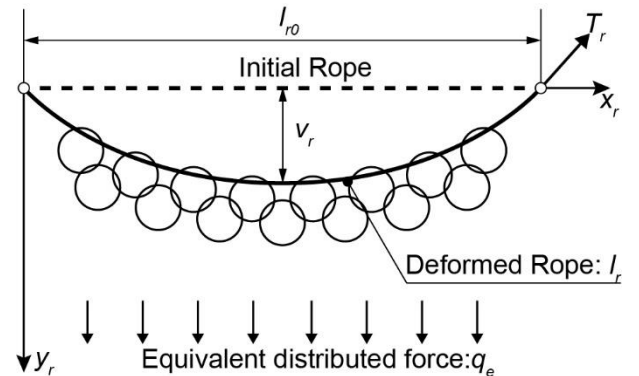

Fig. 15 Deformed wire rope under the traction of the rings

In addition, to further increase the energy absorption capacity of the flexible barrier system, energy dissipating devices are often connected in series at both ends of the wire rope. Such devices usually become effective when the activation

force is attained during the loading process; the brake then maintains this maximum characteristic force F_{energy} and dissipates energy until the maximum brake elongation $\Delta l_{b,\max}$ is developed. Once such a maximum brake stroke is reached, the device loses the capacity to react, and the force in the cable starts to increase again until it fails. The maximum length of the wire rope connected with an energy-dissipating device can reach

$$l_{r,b} = l_{r,\max} + \Delta l_{b,\max} \tag{50}$$

Here, Eq. (47) can be rewritten as follows:

$$l_{r,b} = \sqrt{\frac{l_{r0}^2}{4} + 4v_{r,b}^2} + \frac{l_{r0}^2}{8v_{r,b}} \sinh^{-1}\left(\frac{4v_{r,b}}{l_{r0}}\right) \tag{51}$$

According to Eq. (34), the shortest fibre–spring element first breaks when its axial force equals $\gamma_{N\max}\sigma_y A$; the equivalent spring in this element reaches the maximum elongation. To ensure a consistent maximum deflection v_r with the deformed rope, the stiffness of the springs can be derived by:

$$k_s = \begin{cases} \gamma_{N,\max}\sigma_y A / v_r, & \text{without braker} \\ \gamma_{N,\max}\sigma_y A / v_{r,b}, & \text{with braker} \end{cases} \tag{52}$$
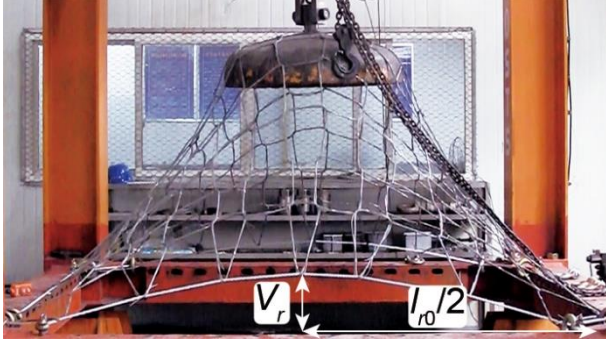
(a) Deformation of the wire rope
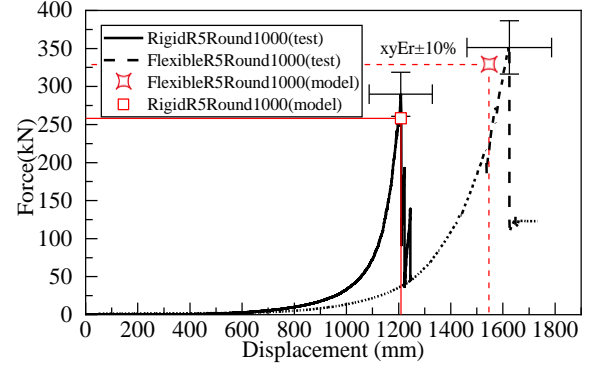
(b) Load-deflection curve

Fig. 16 Punching test of the ring net with flexible boundary

To calibrate the reduction coefficient λ_q of the distributed load along the wire rope, a quasi-static puncture test on a ring net connected with a wire rope was conducted (Test-RN5Rope) (**Fig. 16 a**). The test equipment and instruments conform to **Section 2**. The specification of the net specimen is R5/3.0/300. The size of the square panel is 3.0 m. The wire rope has a diameter of 18 mm, an initial length of 3.0 m at each side of the net boundary, and Young's modulus of 60 GPa [10,12,31].

Fig. 16 a shows the deflection of the wire rope and ring net at the limit state. Observably, the deformation patterns of the steel rings in the ring net are similar between puncture tests with rigid and flexible boundaries. The deformed wire rope has a parabolic shape. Due to the non-linear deformation of the wire rope itself, the maximum out-of-plane deflection, load-bearing, and energy dissipated of the ring net with a flexible boundary have been significantly increased compared with the rigid boundary.

Under out-of-plane loading centrally by a hemispherical-shaped press with a diameter of 1.0 m, the wire-ring net specimens were punctured upwards till failure. Since no energy dissipating device is connected with the wire rope, the maximum deflection v_r of the wire rope in Eq. (45) is used to compute the equivalent stiffness.

The reduction coefficient λ_q from 0 to 1 was tested until $\lambda_q = 0.25$, where the calculated results of the maximum deflection, load-bearing, and energy absorption capacity properly agreed with the test results (**Fig. 16 b**).

6. Verification and discussion

In this section, quasi-static puncture and dynamic destructive tests of the steel ring net panels were conducted. Then, a 1500-kJ full-scale test of the rockfall barrier is presented to validate the potential predicting capability of the analytical model extended to actual flexible barriers.

Table 4
Test specimens and loaded areas

Test	Loaded area		Ring net size	
	Shape	Size	Specimens	Length × width
Test-Po10R7	Polygon	1.0m	R7/300/3.0	3.0m×3.0m
Test-Po06R7	Polygon	0.6m	R7/300/3.0	3.0m×3.0m
Test-Ro10R7	Round	1.0m	R7/300/3.0	3.0m×3.0m
Test-Ro10R5	Round	1.0m	R5/300/3.0	3.0m×3.0m
Test-Ro06R5	Round	0.6m	R5/300/3.0	3.0m×3.0m

6.1. Model validation by quasi-static testing data

Five quasi-static puncture tests were conducted on the ring net with different specifications, loaded area sizes, and shapes. **Table 4** shows the major information on the test specimens and loaded areas.
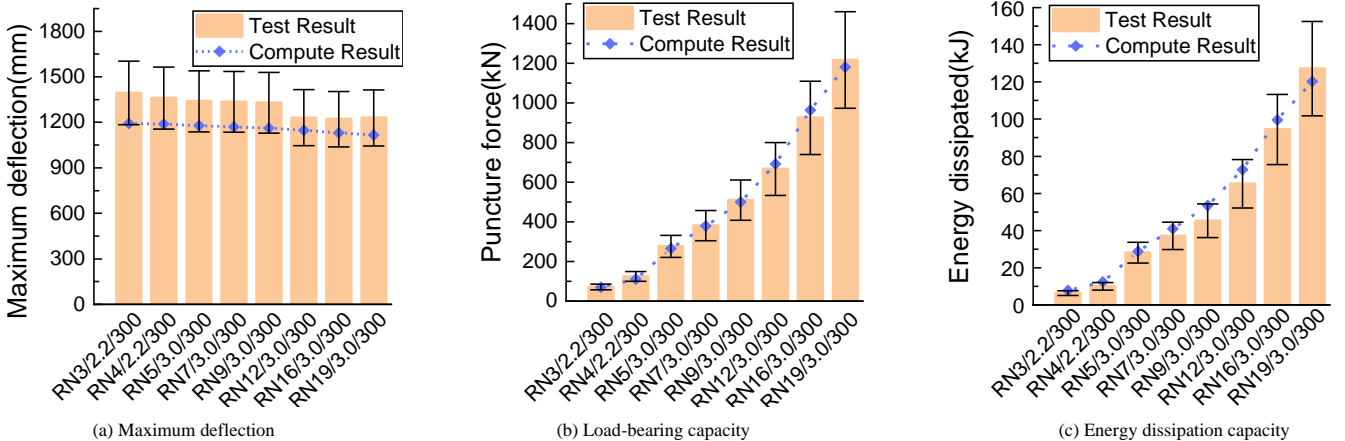

(a) Maximum deflection

(b) Load-bearing capacity

(c) Energy dissipation capacity

Fig. 17 Comparison between the calculation results and punching test results for maximum force and deflection
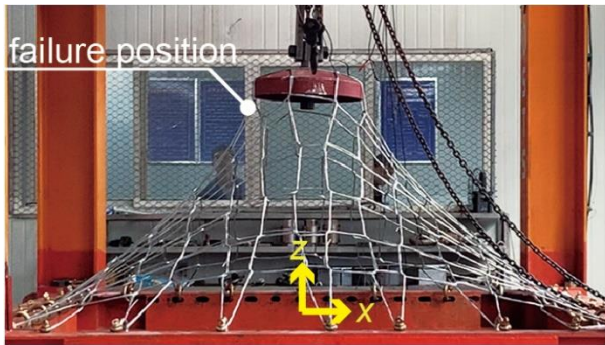
6.1.1. Validation of steel ring specification

To verify the capability of the model for predicting the effect of ring specification, puncture test results of the ring nets with different numbers of winding and steel wire diameters were compared with computational results (**Fig. 17**). With the increase in the number of ring windings, the maximum deflection of the ring nets shows a slightly decreasing trend, while the braking force and energy absorption shown a significantly increasing trend. The maximum relative errors between the experimental and computational results of the deflection, load-bearing, and energy absorption capacity of the ring net are 14.4%, 10.4%, and 14.8%, respectively. The result comparison presented demonstrates the accuracy and reliability of the analytical model developed in this study. Emphatically, adding to the factors affecting the performance of the steel ring net considered in this study, the slippage between the steel wires and the clip, the initial stress of the steel wire section, and the error of the steel ring diameter will also affect the structural performance indicators of the ring net. There are accidental errors in the manufacturing and installation procedures of the ring net, which make the test results more discrete. It is difficult to further improve the calculation accuracy of the flexible ring net.
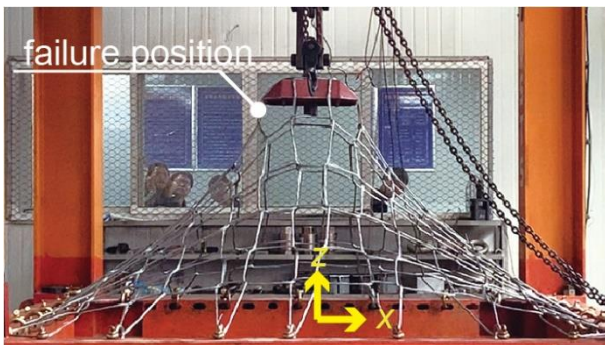
6.1.2. Validation of the loaded area

To validate the capability of the model for predicting the effect of loading area shape, two puncture tests were conducted on R7/3.0/300 net panels loaded by 1000 mm spherical-shaped and polyhedral-shaped presses, respectively. The outer contour of the polyhedral-shaped press has a circumscribed circle with a diameter of 1000 mm. The test results were compared with the analytical model(**Fig. 18 a, b**). Since the polyhedral-shaped press is slightly smaller than the spherical-shaped press, the maximum deflection of the ring net loaded by the 1000 mm polyhedral-shaped press is more significant than the other one. Notably, compared with the spherical press, although the steel wire rings at polyhedral-press edges have undergone an extra bending deformation (curvature radius of $(1/\rho_1)$), the bending degree is relatively more minor compared to the wire at the contact position between the steel rings (curvature radius of $1/\rho_2$). The steel rings first failed at the edge of the loading area instead of the polyhedral edge. Therefore, unless there is a very sharp edge of the polyhedral-shaped press, making the most unfavourable loading condition for steel rings, the effect of the press shape on the structural performance of the ring net is not significant.
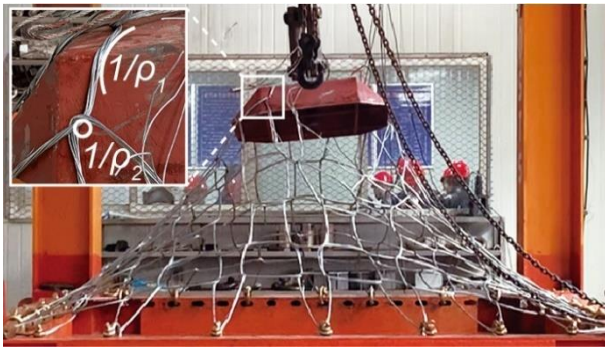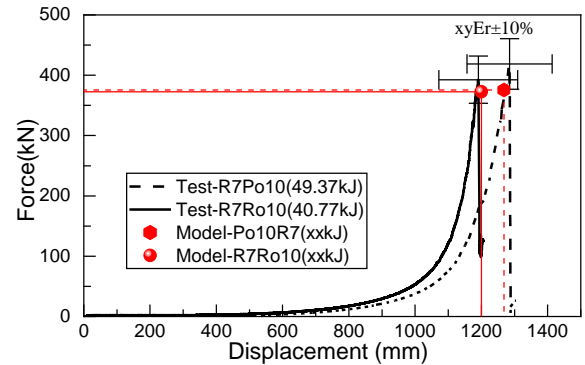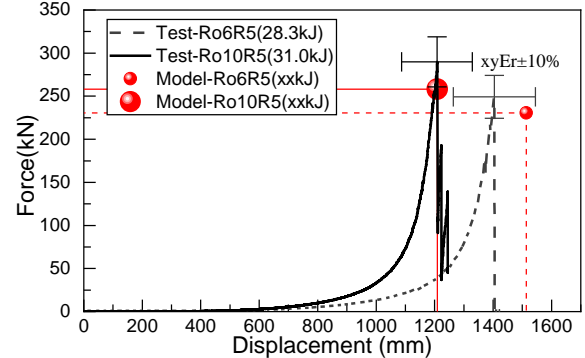

(a) Polygonal-shaped press with size of 1000mm

(b) Force-displacement curve of Po10R7 and He10R7

(c) Hemispherical-shaped press with size of 600mm

(d) Force-displacement curve of He06R5 and He10R5

(e) Polygonal-shaped press with size of 600mm
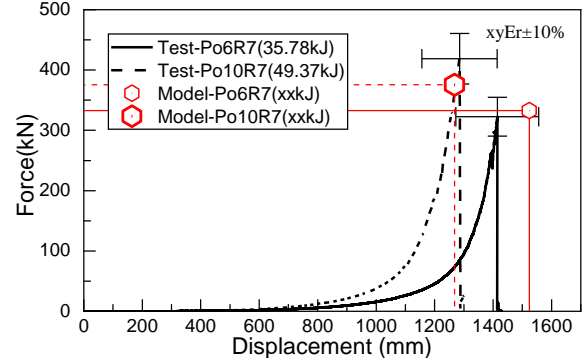
(f) Force-displacement curve of Po06R7 and Po10R7

Fig. 18 Puncture tests on the ring net loaded by different block shape and size

To validate the capability of the model for predicting the effect of the loading area size, puncture tests on an R5/3.0/300 net panel loaded by hemispherical-shaped presses with 600 mm and 1000 mm diameters were conducted (**Fig. 18 c**). Considering another factor, the number of windings n_w, puncture tests on R7/3.0/300 net panels loaded by polygonal-shaped presses with 600 mm and 1000 mm sizes were conducted (**Fig. 18 e**).

The test results were compared with the analytical model (**Fig. 18 d** and **Fig. 18 f**). Concurrently, because of the smaller number of fibre–spring elements in the net loaded by a smaller press size of 600 mm, the load-bearing capacity of the ring net is lower than, which is loaded by a larger press size of 1000 mm.

Since the initial length of the shortest fibre–spring element under 600 mm press loading exceeds the net under 1000 mm press loading, the maximum deflection of the former net exceeds the latter. Observably, the analytical model can reflect the effect tendency of the load area size, and the relative errors in maximum deflection and load-carrying capacity between the test results and calculated results by the analytical model are within 10%. Thus, the analytical model can describe the maximum deflection, load-bearing capacity, and of the ring net with different shapes and sizes of the loaded areas.

6.2. Model validation by dynamic testing data

In actual flexible protection barriers, the ring net is usually subjected to falling rock impact. The load rate of a flexible barrier in static and dynamic conditions differs. The variation in material strength with applied load rate should be considered in designing flexible barriers subjected to suddenly applied loads. From a dynamic plasticity viewpoint, the difference in material behaviour under impact loading and quasi-static loading is that the dynamic strength or yield stress increases as the strain rate increases. The approximate increases in the strain rate are $\dot{\varepsilon} \simeq 1 s^{-1}$ and $10^{-4} s^{-1} \leq \dot{\varepsilon} \leq 10^{-1} s^{-1}$ in quasi-static and drop tests, respectively [37]. Generally, the production material of the wire-ring net in the flexible barrier is a high-strength steel wire with a yield strength exceeding 1770 MPa. The strain rate dependency of the yield stress for high strength wires can be neglected for the strain rates involved in the rockfall problems, typically ranging in $10^{-4} s^{-1} : 10^2 s^{-1}$ [20]. In this range of strain rates, high-strength steel alloys experience only modest degrees of strain-rate sensitivity [38]. In this section, destructive impact tests on two square ring nets have been conducted and compared with the analytical results. The model's ability in yielding consistent results when implemented at the structure scale has also been assessed, based on the data of full-scale impact tests on a 1500kJ-energy rockfall barrier.

### 6.2.1. Validation at net panel scale

Firstly, relevant research results of the ring nets impacted by different specifications, loaded areas are summarised. The net specimens are 3m × 3m in size. The maximum deflection, equivalent load, and energy absorption of the ring nets are compared with the calculation results (**Table 5**). Notably, all the ring nets studied in the literature were neither punctured nor were apparent failures found in the steel rings. Their maximum safe bearing capacity remained partially developed. Therefore, the maximum deflection, load-bearing, and energy absorption capacities predicted by the analytical model exceeded the test results obtained from the references. The positive differences between the calculated and referenced values imply that these ring nets still have a residual bearing capacity after being impacted.

To further verify the capability of the analytical model for predicting the maximum deflection, load-bearing, and energy absorption capacity of the ring net under the impact, two destructive impact tests of R5/3.0/300 and R7/3.0/300 ring nets were performed **Fig. 19**. The net specimen tested has a rectangular shape with a size of 3.9 m. Rigid shackles were used to connect the ring net to the steel frame structure. The length and width of the frame were both 4.65 m, and the height was 4.12 m. A spherical-shaped block with a mass of 760 kg and a diameter of 0.8 m was lifted to 13 m to produce kinetic energy equal to 97.2 kJ. Using a high-speed camera with a sampling frequency of 1000 fps, the vertical displacement–time curve of the block was tracked directly from the high-speed video using image tracking software [39]. The block's velocity was obtained by taking the derivative of a displacement with respect to time. The block's acceleration is recorded by an acceleration sensor installed inside its inner space. All measurements were made using calibration factors (mm/pixel) for each set of frames based on the width of the block. However, small oscillations in the block's position (due to image resolution and vibrations) were amplified by the differentiation step, inducing oscillating velocities. Consequently, the velocity plot was smoothed to avoid noisy data caused by the adjacent averaging method.
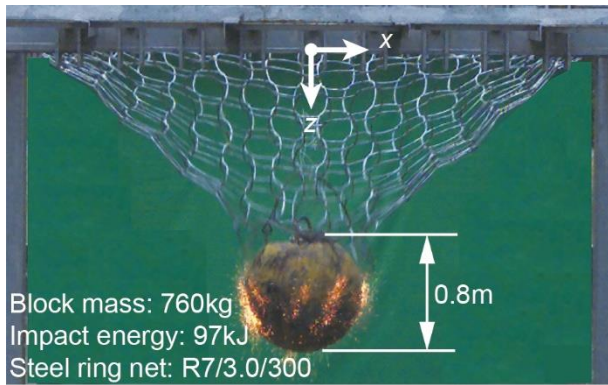
(a) Failure of the ring net under impact load
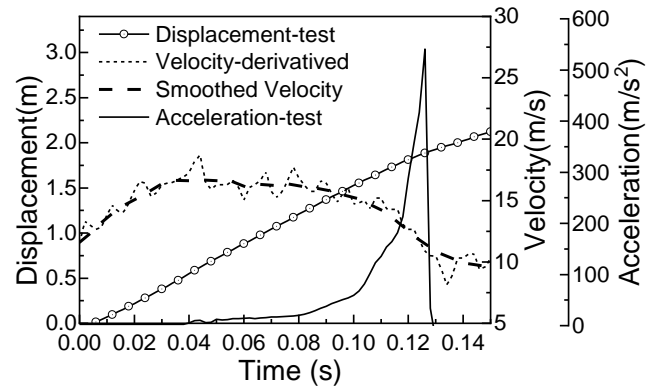
(b) Displacement, velocity, and acceleration time history curve

Fig. 19 Destructive impact test on the ring net

The maximum deflection was obtained directly from the photographs using a reference length. The equivalent load-bearing capacity was calculated as the product of the block mass by its maximum deceleration when the failure occurred. The energy absorption capacity was calculated as the difference in the mechanical energy (including both kinetic energy and potential energy) of falling blocks before and after contact with the ring net. Experimental results from both previous works and the destructive impact test of the ring net are modelled and compared with the calculated results in

Table 5. Observably, the analytical model can satisfactorily predict failure and provide the maximum deflection, load-bearing, and energy absorption capacity of the ring net. The comparisons also add to the evidence that the load rate effect of the ring nets, made by high-strength steel wires, can be neglected in the rockfall problems.

Table 5

Dynamic testing results of the ring net panels

Specimens of ring nets	Fail (Yes/No)	Ring net size	Loading area diameter	Deflection		Equivalent force		Energy dissipated		Reference/Year
				test	model	test	model	test	model	
		length×width	m	m	m	kN	kN	kJ	kJ	
R5/3/300	Yes	3.9m×3.9m	0.8	2.01	1.89	274	263	43.3	46.87	Destructive Impact Test
R7/3/300	Yes	3.9m×3.9m	0.8	1.98	1.87	402	378	59.3	66.67	
R7/3/300	No	3.9m×3.9m	0.8	1.36	1.87	160	378	24	66.67	(Grassl et al. 2002)
R7/3/300	No	3.9m×3.9m	0.8	1.4	1.87	282	378	45	66.67	
R5/3/300	No	3.9m×3.9m	0.8	1.49	1.89	165	263	24.3	46.87	(Volkwein 2004)
R7/3/300	No	3.9m×3.9m	0.8	1.37	1.87	155	378	24.3	66.67	
R12/3/300	No	3.9m×3.9m	0.8	1.33	1.84	128	691	24.3	118.47	
R7/3/300	No	3.9m×3.9m	0.8	1.45	1.87	303	378	44.5	66.67	
R12/3/300	No	3.9m×3.9m	0.8	1.44	1.84	222	691	44.5	118.47	
R5/3/300	No	3.9m×3.9m	0.8	——	1.89	169	221.57	24.3	38.13	(Escallón 2013)

6.2.2. Validation at structure scale

A full-scale impact test and numerical simulation of a rockfall barrier with a maximum energy level of 1500 kJ are used to explore the capability of the analytical model when applied to evaluate the maximum structural performance of the net force. One can refer to [30,40] for a complete description of the test procedure and numerical model of the barrier.

A full-scale impact test on the flexible ring net barrier is shown in **Fig. 20**. The ring chains on the shortest load path of the ring net are fully stretched, and the internal axial force vectors of the rings were balanced with the out-of-plane loading. Large deflection for both the ring net and the flexible boundary is developed in coordination. Steel rings showing the largest deformation on the shortest load path are consistent with deformed ring chains. These rings play an indispensable role in the structural performance of the net.

Under the impact of the 4002 kg block with 1500 kJ kinetic energy, the ring net with a flexible boundary has successfully intercepted the block, and no apparent damage occurred on steel rings. The maximum diameter of the polyhedral block is 1.374 m. The specification of the ring net is R12/3.0/300 with a length of 10 m and a width of 5.5 m. The support rope has a diameter of 22 mm and a broken force of 305 kN. Both ends of the support rope along the span direction are connected in series with two energy dissipaters with a maximum elongation of 1.0 m and a maximum characteristic force of 75 kN.

The same finite element model of the rockfall barrier was developed.

Keeping the same shape and size of the block, the ring net was punctured when the initial impact energy of the block increased to 2000 kJ. The steel rings at the shortest load path broke first, and the maximum normalized axial stress ratio of straightened steel rings in the whole barrier structure is 0.404, which agrees with the axial stress ratio of 0.42 measured through breaking load in the three-ring chain test with the same specification of R12/3.0/300. **Fig. 20** shows the ultimate limit state of the rockfall barrier. There are two specific load paths in the net. The steel rings deformed slightly in load path 1, indicating that a small internal force developed in these rings. The steel rings deformed significantly in the shortest load path 2, which should be viewed as the primary contribution of the load-bearing capacity of the ring net.

The performance curve (force–elongation curve) of the rockfall barrier is shown in **Fig. 20**. Both the maximum structural performance of the experimental and numerical results are compared with the analytical model. Observably, in the rockfall barrier, the ring net's load-bearing capacity calculated by the analytical model is in good consistent with the numerical simulation results. As the analytical model does not consider the rotation of the steel posts and specific arrangement of non-impact spans of the barrier, the maximum deflection is smaller than the numerical calculation results, and the maximum energy absorption is slightly smaller than the numerical results. The relative error between the analytical model and the test results in this work is below 15%. Expectedly, the current accuracy can meet engineering needs.
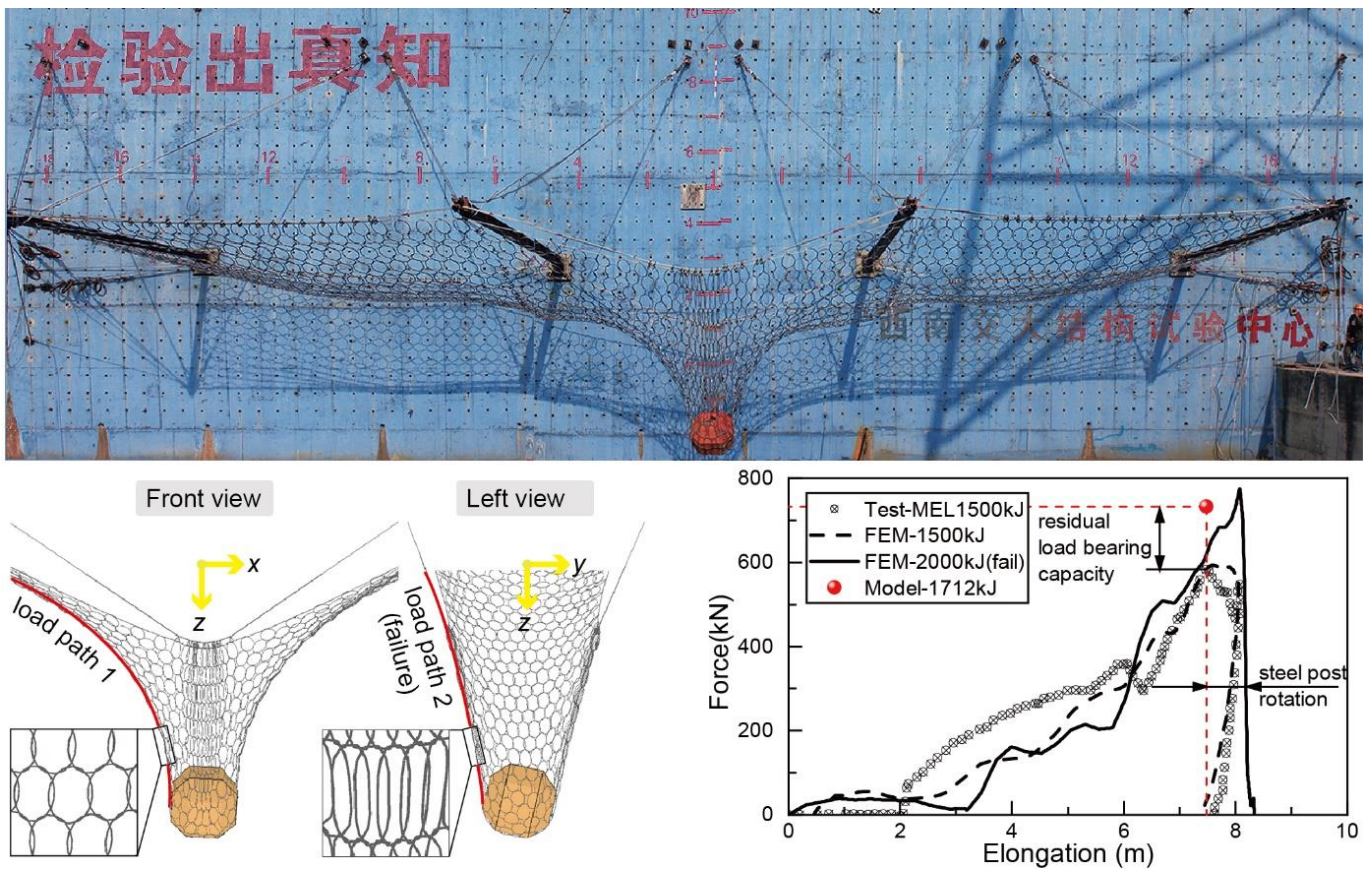

Fig. 20 Full-scale impact test and numerical simulations on a 1500kJ rockfall barrier

6.3. Effect of multiple factors

The deflection, load-bearing, and energy absorption capacity are important structual performance indicators for the design and selection of ring nets. To extend the results of the standard net characterization (i.e. laboratory puncture test) to more general field conditions. The effects of multiple factors, such as the number of windings of steel ring n_w, wire diameter d, loading area size R_p, single ring diameter D, the length-width ratio κ, the boundary stiffness k_s, and the load position are discussed in the following.

Table 6 shows the reference values and ranges of each factor. Notably, to make the parametric analysis results reliable, the load position is set to the net's centre. The reference value of $k_s = 5000$kN/mm is set to be quite large to maintain consistency with the experimental rigid boundary condition. The maximum deflection H, load-bearing capacity F, and energy absorption capacity E of the ring net influenced by various factors are plotted collaboratively with trend lines (**Fig. 21**).

(1) Effect of number of windings n_w

In this perspective, n_w of the wire-ring is varied ranging from 3 to 15 with an incremental step of 2. The other parameters are the same as those in the reference test reported in **Table 6**.

The structural performance indicators of the ring net obtained for seven different values of n_w (3, 5, 7, 9, 11, 13, 15) is reported in **Fig. 21 a**. The maximum out-of-plane deflection slightly decreases with the increasing number of windings n_w. **Fig. 21 a** shows a strong linear correlation between the maximum out-of-plane deflection H and the number of windings. The load-bearing capacity F and the energy absorption E increase obviously with the increasing number of windings, indicating that the n_w limitedly influences the maximum deflection of the ring net, but significantly influences the load-bearing and energy absorption capacity of the ring net.

(2) Effect of wire diameter d

In this perspective, the dimension d of the wire is varied ranging from 0.6 mm to 4.8 mm with an incremental step of 0.6 mm. The other parameters are the same as those in the reference test reported in **Table 6**. The structural performance indicators of the ring net obtained for seven different values of d (1.2 mm, 1.8 mm, 2.4 mm, 3.0 mm, 3.6 mm, 4.2 mm, 4.8 mm) is reported in **Fig. 21 b**. With the increase in wire diameter d, the maximum deflection H of the

ring net decreases linearly, while the load-bearing capacity F and energy absorption capacity E increase, and the rate of increase increases continuously,

indicating that the steel wire diameter limitedly influences the maximum deflection of the ring net but more significantly influences the bearing capacity and energy absorption than the number of windings (**Fig. 21 a**).

Table 6
Main parameters of multiple factors

Parameter type	parameter	unit	range	reference value
Influential Parameters	Number of windings (n_w)	1	3~15	9
	Diameter of single steel wire (d)	mm	1.2~4.8	3.0
	Radius of punching device (R_p)	mm	200~800	500
	Diameter of steel ring (D)	mm	120~480	300
	Length–width ratio (κ)	1	1.0~2.2	1.0
	Boundary stiffness (k_s)	N/mm	2^{-5}~2^{25}	5×10^6
System performance	Out-of-plane deformation capacity (H)	m	——	1.18
	Out-of-plane load capacity (F)	kN	——	504.60
	Energy dissipation capacity (E)	kJ	——	57.16

(3) Effect of steel ring diameter D

In this perspective, steel ring diameter D is varied ranging from 0.2 m to 0.8 m with an incremental step of 0.06 m. The other parameters are the same as those in the reference test reported in **Table 6**. The structural performance indicators of the ring net obtained for seven different values of D (0.12 m, 0.18 m, 0.24 m, 0.30 m, 0.36 m, 0.42 m, 0.48 m) is reported in **Fig. 21 c**. The maximum out-of-plane deflection H slightly increases with the increasing diameter of steel rings. **Fig. 21 c** shows a strong linear correlation between the maximum out-of-plane deflection and the diameter of steel rings. The load-bearing capacity F and energy absorption capacity E decrease with increasing steel ring diameter, indicating that the steel ring diameter limitedly influences the maximum deflection of the ring net, but significantly influences the load-bearing and energy consumption of the ring net.

(4) Effect of loading area size R_p

In this perspective, loading area size R_p is varied ranging from 0.2 m to 0.8 m with an incremental step of 0.1 m. The other parameters are the same as those in the reference test reported in **Table 6**. The structural performance indicators of the ring net obtained for seven different values of R_p (0.2 m, 0.3 m, 0.4 m, 0.5 m, 0.6 m, 0.7 m, 0.8 m) is reported in Fig. **Fig. 21 d**. As the size of the loading area R_p increases, the maximum deflection H of the net decreases linearly, and the bearing capacity F gradually increases, showing a quadratic relationship between them. The larger the loading area, the shorter the initial length of the equivalent fibres along the edge, so the maximum deflection H could be reduced; however, as the loading area increases, the number of force vectors balanced with the out-of-plane loading of the ring net increases, resulting in a larger load-bearing capacity of the ring net. Conversely, the smaller the size of the loading area R_p, the lower the load-bearing capacity F. Thus, the ring net could be more prone to damage with a smaller loading area. This result agrees with the "bullet effect" of the flexible intercepting structure reported in the literature [36,41]. The energy absorption of the ring net first increases and then decreases with the increase in the number of windings of the steel rings. This is because the energy absorption capacity of the ring net positively correlates with deflection and load-bearing capacity. As the loading area increases, the influence of the maximum deflection reduction of the ring net on energy consumption gradually exceeds that of the load-bearing capacity increment on energy absorption capacity.

(5) Effect of length–width ratio κ

In this perspective, length–width ratio κ of the ring net is varied ranging from 1.0 to 2.2 with an incremental step of 0.2. The other parameters are the same as those in the reference test reported in **Table 6**. The structural performance indicators of the ring net obtained for seven different values of κ (1.0, 1.2, 1.4, 1.6, 1.8, 2.0, 2.2) is reported in **Fig. 21 e**. Keeping the width of the rectangular ring net constant (3.0 m), as the length-width ratio increases, the maximum deflection of the ring net slowly increases with a linear trend, while the load-bearing capacity and energy consumption capacity of the ring net significantly decrease

and eventually stabilise, showing an exponential trend (**Fig. 21 e**). The length-width ratio linearly correlates with the maximum deflection of the ring net and exponentially correlates with load-bearing capacity and energy absorption. The length-width ratio of the rectangular net is a key factor affecting the load-bearing and energy-consumption performance of the ring net. When the length-width ratio tends to 1, the ring net can fully perform its protective function.

(6) Effect of boundary stiffness k_s

In this perspective, boundary stiffness k_s of the ring net is varied ranging from 2^{-5} N/mm to 2^{25} N/mm with increasing by multiples of 2. The other parameters are the same as those in the reference test reported in **Table 6**. For clarity, the structural performance indicators of the ring net obtained for eighteen different values of k_s ($2^8 N/mm$ to $2^{25} N/mm$) is reported in **Fig. 21 f**. As the boundary stiffness increases, the maximum deflection and energy absorption capacity decrease exponentially, and the load-bearing capacity of the ring net decreases in the shape of an inverse logistic curve. Since the fibres are connected in series with the equivalent spring, the stiffness of the fibre–spring element in the analytical model increases as the boundary stiffness k_s increases, inducing a smaller elongation of the element and smaller deflection of the net when the failure occurs.

When the boundary stiffness is below 0.256 kN/mm, the load-bearing capacity remains constant because once the boundary stiffness is reduced to a certain level, the direction of the internal force vectors of the fibre–spring elements are almost parallel to the loading direction. However, the maximum axial force of the fibre–spring element remains constant $\gamma_{Nmax}\sigma_y A$.

When the boundary stiffness exceeds 0.256 kN/mm and is below 5000 kN/mm, the structural performance indicators of the net are very sensitive to the boundary stiffness. As the boundary stiffness increases, the maximum deflection and energy absorption capacity decrease exponentially, and the reduction rate of the load-bearing capacity increases first and then decreases to zero.

When the boundary stiffness exceeds 5000 kN/mm, the net boundary is considered a rigid boundary, and the structural performance indicators of the net tend to be stable.

Fig. 21 f shows that the maximum deflection, load-bearing, and energy absorption capacity of the ring net with a rigid boundary are the smallest under the centrally loading conditions — considered as the lower bound of the structural performance of the ring net with flexible boundary. In practical rockfall barriers, wire ropes are often used as the flexible boundary of the ring net, and energy-dissipating devices with a certain elongation capacity are attached to the ends of the wire ropes. From the analytical method viewpoint, these technical measures significantly reduce the boundary stiffness and increase the maximum deflection of the net while concurrently adjusting the direction of the fibre–spring elements to be parallel with the out-of-plane loading direction to increase the load-carrying capacity. Further, greater deflection and load-bearing capacity will increase the energy absorption capacity of the ring net.
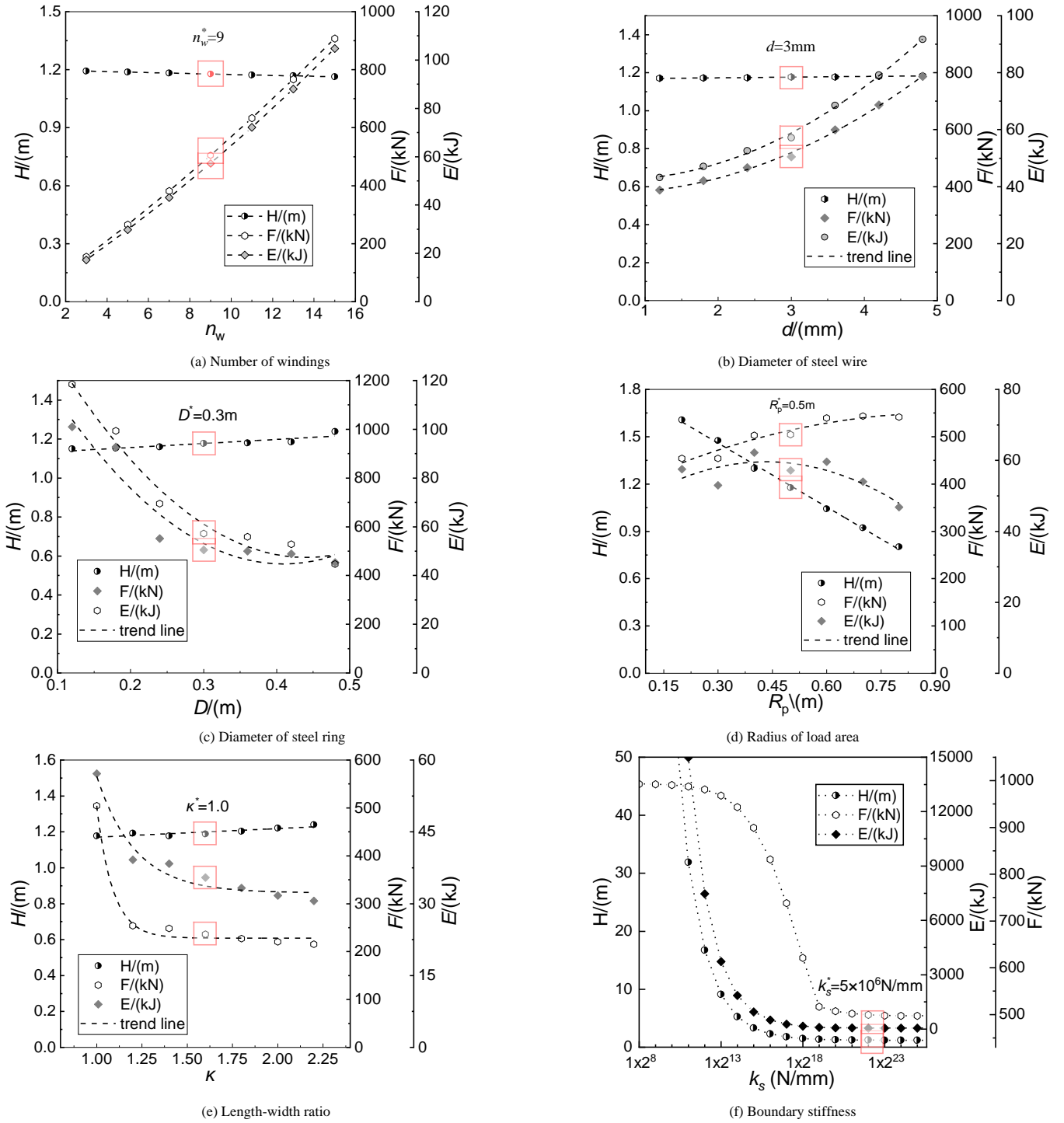
(a) Number of windings

(b) Diameter of steel wire

(c) Diameter of steel ring

(d) Radius of load area

(e) Length-width ratio

(f) Boundary stiffness

Fig. 21 Structural performance indicators of ring nets influenced by multiple factors

(7) Effect of the load position

The effect of a generic loaded position (e_x, e_y) on the structural performance indicators of the ring net panel can be observed in the contour plots of **Fig. 22**. The square net panel size is 3 m, with a steel ring specification of R9/3.0/30. The spherical press diameter is 1 m. As described in Eq. (34), the shorter the initial length of the fibre–spring element, the greater the axial force at a certain out-of-plane deflection. The structural performance of the net panel is controlled by the shortest fibre–spring element on which failure occurs first.

Fig. 22 shows that, when the loading position is located at the geometry centre of the net panel, the structural performance indicators of the ring net reach their maximum. When the load is applied close to the net's boundary, the length of the fibre–spring elements at the shortest load path decreases. Therefore, the

deflection, load-bearing, and energy consumption capacity decrease to varying degrees.

Due to the symmetry of the ring net in the xy plane, the structural performance indicators also show symmetrical properties with the shift of loading position. When the loading position is on the symmetrical axes, the ring net has at least two shortest load paths when it fails. When the loading area deviates from the symmetrical axes, the ring net has only one shortest load path when it fails, and there are fewer fibre–spring elements broken simultaneously. When the loading position is located on the four symmetrical axes, the structural performance indexes slowly decrease with an increase in the eccentric distance of the loading position centre. However, all structural performance indicators fall rapidly when the loading position deviates from the symmetric axes.
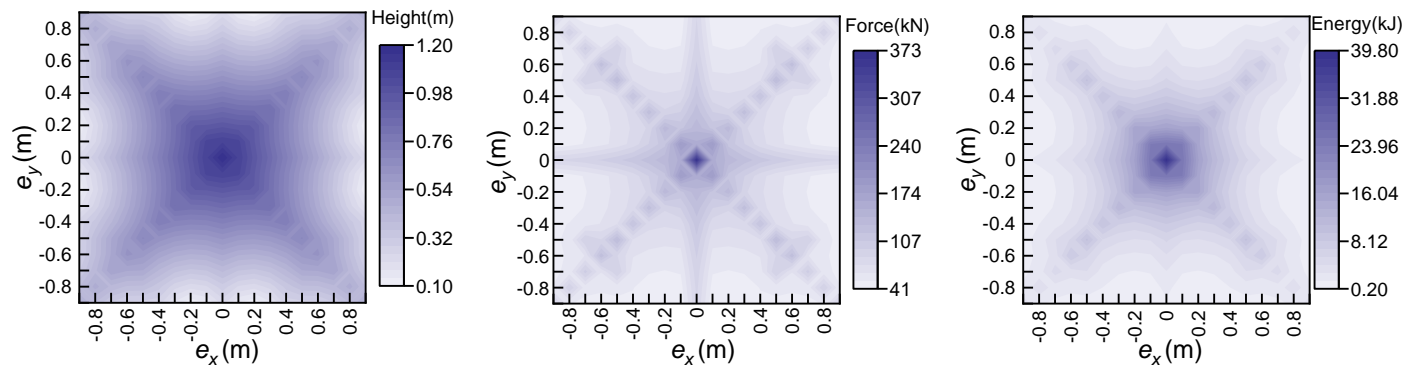
Fig. 22 Effect of the load position

Conclusion

This work investigates the maximum deflection, load-bearing, and energy absorption capacity of steel wire-ring nets considering multiple factors' influence. The experimental results indicate that the ring net's structural performance was affected specifically by ring chains on the shortest load path. Before breaking, the steel wire of each ring underwent coupled tension–bending deformation. Further correlation analyses have shown that three structural performance indicators between ring nets and ring chains were strongly related. Accordingly, the ring chains on the load path of the ring net were equivalent to the fibre–spring elements. A three-dimensional analytical model was established. Explicit expressions were derived, which is convenient for engineering design and application. Comprehensive quasi-static and dynamic destructive tests on thirty-two ring nets are conducted to validate the proposed approach. The relative error between the calculation results and the test results was less than 15%, verifying the model's reliability.

Subsequently, the analytical model was used to perform a parametric analysis aimed at quantifying the influence of the fundamental parameters characterizing the field conditions. The main results are summarized as follows:

The number of windings controls the load-bearing and energy absorption capacity of the ring net. However, it has a negligible effect on the panel's maximum deflection.

The steel wire diameter influences the bearing capacity and energy absorption of the ring net more significantly than the number of windings but limitedly influences the maximum deflection H. The maximum deflection H of ring net decreases linearly with the increase in wire diameter d. The load-bearing and energy absorption increase with the wire diameter near exponential growth.

The wire-ring diameter is one key factor influencing the total number of fibre–spring elements in the analytical model (Eqs. (16) and (17)). It significantly influences the load-bearing and energy absorption capacity, but slightly influences the maximum deflection of the ring net.

The loaded area size is another key factor influencing the total number of fibre–spring elements (Eq. (17)). The larger the loading area, the shorter the initial length of the equivalent fibres along the edge, so the maximum deflection H could be reduced. However, as the loading area increases, the number of force vectors balanced with the out-of-plane loading of the ring net increases, resulting in a larger load-bearing capacity of the ring net. Under the influence of maximum deflection and load-bearing capacity, The energy absorption of the ring net first increases and then decreases with the increase in the number of windings of the steel rings.

The loaded area shape affects the deformation characteristics of the steel wires at the edges of the loaded area. Compared with the spherical press, the steel wire rings at polyhedral-press edges have undergone an extra bending deformation in the puncture test of the ring net. However, unless there is a very sharp edge of the polyhedral-shaped press, making a more unfavourable condition than contact points between the steel rings, the effect of the loaded area shape on the structural performance of the ring net is not significant.

The load position affects the symmetrical properties of the steel rings distributed on the shortest load paths. When the loading area deviates from the symmetrical axes, the ring net has only one shortest load path when it fails, and there are fewer fibre–spring elements broken simultaneously. All of the maximum deflection, load-bearing, and energy absorption capacity reached the highest value when the loaded area is located at the centre of the ring net.

The length–width ratio controls the maximum deflection and symmetrical properties of the ring net. Keeping the width of the rectangular ring net constant, as the length-width ratio increases, the deflection of the ring net slowly increases with a linear trend, while the load-bearing and energy absorption capacity of the ring net significantly decrease and eventually stabilise, showing an exponential trend. When the length-width ratio tends to 1, the ring net can fully perform its protective function.

The boundary stiffness plays a crucial role in the structural performance of the ring net. When the boundary stiffness exceeds 0.256 kN/mm and is below 5000 kN/mm, the structural performance indicators of the net are very sensitive to the boundary stiffness. Once the boundary stiffness is below 0.256 kN/mm, the load-bearing capacity remains constant. When the boundary stiffness exceeds 5000 kN/mm, the net boundary is considered a rigid boundary, and all of the structural performance indicators of the net tend to be stable. The maximum deflection, load-bearing, and energy absorption capacity of the ring net with a rigid boundary are the lower bound of the structural performance of the ring net with a flexible boundary.

The Load rates of a flexible barrier in quasi-static and dynamic conditions differ. However, for the strain rates involved in rockfall problems, the approximate increases in the strain rates range from $10^{-4}s^{-1}$ to $10^{2}s^{-1}$. In this range of strain rates, ultra-high-strength steel wires experience only modest degrees of strain-rate sensitivity and the strain rate effect of the material can be neglected.

In practice, all indicators of maximum deflection, load-bearing, and energy absorption capacity of the ring net should be carefully set to satisfy engineering requirements during designing. The more sensitive factor should be primarily adjusted to realize fast and effective control of ring net structural performance indicators.

Acknowledgements

References

[1] Gentilini C., Gottardi G., Govoni L., Mentani A. and Ubertini F., "Design of falling rock protection barriers using numerical models", Engineering Structures, 50, 96-106, 2013. https://doi.org/10.1016/j.engstruct.2012.07.008

[2] Volkwein A. and Gerber W., "Stronger and lighter-evolution of flexible rockfall protection systems", London Symposium Report: Taller, Longer, Lighter (IABSE-IASS 2011), Zurich, Switzerland, 1-5, 2011.

[3] Kwan J.S.H., Chan S.L., Cheuk J. C. Y. and Koo R. C. H., "A case study on an open hillside landslide impacting on a flexible rockfall barrier at Jordan Valley, Hong Kong", Landslides, 11(6), 1037–1050, 2014. https://doi.org/10.1007/s10346-013-0461-x

[4] Wendeler C. and Volkwein A., "Laboratory tests for the optimization of mesh size for flexible debris-flow barriers", Natural Hazards and Earth System Sciences, 15(12), 2597-2604, 2015. https://doi.org/10.5194/nhess-15-2597-2015

[5] Liu, C., Yu Z.X. and Zhao S.C. "Quantifying the impact of a debris avalanche against a flexible barrier by coupled DEM-FEM analyses", Landslides, 17, 33-47, 2019. https://doi.org/10.1007/s10346-019-01267-8

[6] Margreth S. and Roth A., "Interaction of flexible rockfall barriers with avalanches and snow pressure", Cold Regions Science and Technology, 51(2), 168-177, 2008. https://doi.org/10.1016/j.coldregions.2007.03.008

[7] Zhao S.C., Yu Z.X., Zhao L., Qi X. and Wei T., "Damage mechanism of rockfall barriers under strong impact loading", Engineering Mechanics (in Chinese), 33(10), 24-34, 2016.

[8] von Boetticher A. and Volkwein A., "Numerical modelling of chain-link steel wire nets with discrete elements", Canadian Geotechnical Journal, 56(3), 398–419, 2018. https://doi.org/10.1139/cgj-2017-0540

[9] Sasiharan N., Muhunthan B., Badger, T. C., Shu S. and Carradine D. M., "Numerical analysis of the performance of wire mesh and cable net rockfall protection systems", Engineering Geology, 88(1), 121-132, 2006. https://doi.org/10.1016/j.enggeo.2006.09.005

[10] Castro-Fresno D., del Coz Diaz J. J., López L. A. and García Nieto P. J., "Evaluation of the resistant capacity of cable nets using the finite element method and experimental validation."

Engineering Geology, 100(1), 1–10, 2008. https://doi.org/10.1016/j.enggeo.2008.02.007

[11] Tahmasbi S., Giacomini A., Wendeler C. and Buzzi O., "Towards a novel and efficient method to determine the failure energy of rockfall chain-link meshes", Computers and Geotechnics, 119, 103299, 2020. https://doi.org/10.1016/j.compgeo.2019.103299

[12] Bertrand D., Trad A., Limam A. and Silvani C., "Full-Scale Dynamic Analysis of an Innovative Rockfall Fence Under Impact Using the Discrete Element Method: from the Local Scale to the Structure Scale", Rock Mechanics and Rock Engineering, 45(5), 885–900, 2012. https://doi.org/10.1007/s00603-012-0222-5

[13] Volkwein A., Roth A., Gerber W. and Vogel A. "Flexible Rockfall Barriers Subjected to Extreme Loads", Structural Engineering International, 19(3), 327–332, 2009. https://doi.org/10.2749/101686609788957900

[14] Grassl H. G., Volkwein A., Anderheggen E. and Ammann W., "Steel-net rockfall protection-experimental and numerical simulation", WIT Transactions on The Built Environment, 63, 143–153, 2002.

[15] Volkwein A., "Numerische Simulation von flexiblen Steinschlagschutzsystemen", Doctoral Thesis, ETH Zürich, Switzerland, 2004.

[16] Buzzi O., Spadari M., Giacomini A., Fityus S. and Sloan S. W., "Experimental Testing of Rockfall Barriers Designed for the Low Range of Impact Energy", Rock Mechanics and Rock Engineering, 46(4), 701–712, 2013. https://doi.org/10.1007/s00603-012-0295-1

[17] Yu Z.X., Liu, C., Guo L.P., Zhao L. and Zhao S.C., "Nonlinear Numerical Modeling of the Wire-Ring Net for Flexible Barriers", Shock and Vibration, 7934696, 2019. https://doi.org/10.1155/2019/3040213

[18] Nicot F., Cambou B. and Mazzoleni G., "From a constitutive modelling of metallic rings to the design of rockfall restraining nets", International Journal for Numerical and Analytical Methods in Geomechanics, 25, 49-70, 2001. https://doi.org/10.1002/1096-9853(200101)25:1<49::AID-NAG117>3.0.CO;2-N

[19] Gentilini C., Govoni L., de Miranda S., Gottardi G. and Ubertini F., "Three-dimensional numerical modelling of falling rock protection barriers", Computers and Geotechnics, 44, 58-72, 2012. https://doi.org/10.1016/j.compgeo.2012.03.011

[20] Escallón J. P., Wendeler C., Chatzi E. and Bartelt P., "Parameter identification of rockfall protection barrier components through an inverse formulation", Engineering Structures, 77, 1-16, 2014. https://doi.org/10.1016/j.engstruct.2014.07.019

[21] Brighenti R., Segalini A. and Ferrero A.M., "Debris flow hazard mitigation: A simplified analytical model for the design of flexible barriers", Computers and Geotechnics, 54, 1-15, 2013. https://doi.org/10.1016/j.compgeo.2013.05.010

[22] Ferrero A. M., Segalini A. and Umili G., "Experimental tests for the application of an analytical model for flexible debris flow barrier design", Engineering Geology, 185, 33-42, 2015. https://doi.org/10.1016/j.enggeo.2014.12.002

[23] Spadari M., "Experimental and numerical investigations on barriers for rockfall hazard mitigation", Doctoral Thesis, University of Newcastle, 2013.

[24] Hambleton J. P., Buzzi O., Giacomini A., Spadari M. and Sloan S. W., "Perforation of Flexible Rockfall Barriers by Normal Block Impact", Rock Mechanics and Rock Engineering, 46(3), 515–526, 2013. https://doi.org/10.1007/s00603-012-0343-x

[25] Peila D., Pelizza S. and Sassudelli F., "Evaluation of Behaviour of Rockfall Restraining Nets by Full Scale Tests", Rock Mechanics and Rock Engineering, 31(1), 1-24, 1998. https://doi.org/10.1007/s006030050006

[26] Yu Z.X., Qiao Y.K., Zhao L., Xu H., Zhao S.C. and Liu Y.P., "A simple analytical method for evaluation of flexible rockfall barrier Part 1: working mechanism and analytical solution", Advanced Steel Construction, 14(2), 115–141, 2018a. https://doi.org/10.18057/IJASC.2018.14.2.1

[27] Yu Z.X., Qiao Y.K., Zhao L., Xu H., Zhao S.C. and Liu Y.P., "A simple analytical method for evaluation of flexible rockfall barrier Part 2:application and full-scale test", Advanced Steel Construction, 14(2), 142-165, 2018b. https://doi.org/10.18057/IJASC.2018.14.2.2

[28] Guo L.P., Yu Z.X., Luo L.R., Qi X. and Zhao S.C., "An analytical method of puncture mechanical behavior of ring nets based on the load path equivalence", Engineering Mechanics (in Chinese), 37(5), 129–139, 2020. https://doi.org/10.6052/j.issn.1000-4750.2019.07.0345

[29] Trad A., Limam A., Bertrand D. and Robit P., "Multi-scale Analysis of an Innovative Flexible Rockfall Barrier", Rockfall Engineering, John Wiley & Sons, Ltd, 303-342, 2013. https://doi.org/10.1002/9781118601532.ch9

[30] Xu H., Gentilini C., Yu Z.X., Qi X. and Zhao S.C., "An energy allocation based design approach for flexible rockfall protection barriers", Engineering Structures, 173, 831-852, 2018. https://doi.org/10.1016/j.engstruct.2018.07.018

[31] Mentani A., Giacomini A., Buzzi O., Govoni L., Gottardi G. and Fityus S., "Numerical Modelling of a Low-Energy Rockfall Barrier: New Insight into the Bullet Effect", Rock Mechanics and Rock Engineering, 49(4), 1247–1262, 2016. https://doi.org/10.1007/s00603-015-0803-1

[32] Zhu Z. H., Yin J. H., Ouyang C., Tan D. Y. and Qin J.Q., "Modeling a Flexible Ring Net with the Discrete Element Method", Journal of Engineering Mechanics, 146(2), 04019120. 2020. https://doi.org/10.1061/(ASCE)EM.1943-7889.0001707

[33] Steel wire ring net panels–Definitions and specifications. ISO 17745:2016, 16, 2016.

[34] Falling Rock Protection Kits, European Assessment Document–EAD 340059-00-0106 EOTA, 2018.

[35] Jirasek M. and Bazant Z. P., Inelastic Analysis of Structures, John Wiley & Sons, England, 2001.

[36] Spadari M., Giacomini A., Buzzi O. and Hambleton J. P., "Prediction of the Bullet Effect for Rockfall Barriers: a Scaling Approach", Rock Mechanics and Rock Engineering, 45(2), 131–144, 2012. https://doi.org/10.1007/s00603-011-0203-0

[37] Cristescu N.D., Dynamic Plasticity, World Scientific Publishing Co. Pte. Ltd., University of Florida, USA, 2007.

[38] Boyce B. L. and Dilmore M.F., "The dynamic tensile behavior of tough, ultra-high-strength steels at strain-rates from 0.0002s−1 to 200s−1", International Journal of Impact Engineering, 36(2), 263–271, 2009. https://doi.org/10.1016/j.ijimpeng.2007.11.006

[39] Xcitex. Xcitex - ProAnalyst Motion Analysis Software. Proanalyst. (2021).

[40] Yu Z.X., Zhao L., Liu Y.P., Zhao S.C., Xu H. and Chan S.L., "Studies on flexible rockfall barriers for failure modes, mechanisms and design strategies: a case study of Western China", Landslides, 16(2), 347–362, 2019. https://doi.org/10.1007/s10346-018-1093-y

[41] Buzzi O., Leonarduzzi E., Krummenacher B., Volkwein A. and Giacomini A., "Performance of High Strength Rock Fall Meshes: Effect of Block Size and Mesh Geometry", Rock Mechanics and Rock Engineering, 48(3), 1221–1231, 2015. https://doi.org/10.1007/s00603-014-0640-7